Acta Oceanol. Sin., 2021, Vol. 40, No. 11, P. 11–30
https://doi.org/10.1007/s13131-021-1830-2
http://www.aosocean.com
E-mail: ocean2@hyxb.org.cn

Observations and modelling of the travel time delay and leading negative phase of the 16 September 2015 Illapel, Chile tsunami

Peitao Wang[1]*, Zhiyuan Ren[1], Lining Sun[1], Jingming Hou[1], Zongchen Wang[1], Ye Yuan[1], Fujiang Yu[1]

[1] Key Laboratory of Marine Hazards Forecasting, National Marine Environmental Forecasting Center, Ministry of Natural Resources, Beijing 100081, China

Received 21 November 2020; accepted 23 February 2021

Abstract

The systematic discrepancies in both tsunami arrival time and leading negative phase (LNP) were identified for the recent transoceanic tsunami on 16 September 2015 in Illapel, Chile by examining the wave characteristics from the tsunami records at 21 Deep-ocean Assessment and Reporting of Tsunami (DART) sites and 29 coastal tide gauge stations. The results revealed systematic travel time delay of as much as 22 min (approximately 1.7% of the total travel time) relative to the simulated long waves from the 2015 Chilean tsunami. The delay discrepancy was found to increase with travel time. It was difficult to identify the LNP from the near-shore observation system due to the strong background noise, but the initial negative phase feature became more obvious as the tsunami propagated away from the source area in the deep ocean. We determined that the LNP for the Chilean tsunami had an average duration of 33 min, which was close to the dominant period of the tsunami source. Most of the amplitude ratios to the first elevation phase were approximately 40%, with the largest equivalent to the first positive phase amplitude. We performed numerical analyses by applying the corrected long wave model, which accounted for the effects of seawater density stratification due to compressibility, self-attraction and loading (SAL) of the earth, and wave dispersion compared with observed tsunami waveforms. We attempted to accurately calculate the arrival time and LNP, and to understand how much of a role the physical mechanism played in the discrepancies for the moderate transoceanic tsunami event. The mainly focus of the study is to quantitatively evaluate the contribution of each secondary physical effect to the systematic discrepancies using the corrected shallow water model. Taking all of these effects into consideration, our results demonstrated good agreement between the observed and simulated waveforms. We can conclude that the corrected shallow water model can reduce the tsunami propagation speed and reproduce the LNP, which is observed for tsunamis that have propagated over long distances frequently. The travel time delay between the observed and corrected simulated waveforms is reduced to <8 min and the amplitude discrepancy between them was also markedly diminished. The incorporated effects amounted to approximately 78% of the travel time delay correction, with seawater density stratification, SAL, and Boussinesq dispersion contributing approximately 39%, 21%, and 18%, respectively. The simulated results showed that the elastic loading and Boussinesq dispersion not only affected travel time but also changed the simulated waveforms for this event. In contrast, the seawater stratification only reduced the tsunami speed, whereas the earth's elasticity loading was responsible for LNP due to the depression of the seafloor surrounding additional tsunami loading at far-field stations. This study revealed that the traditional shallow water model has inherent defects in estimating tsunami arrival, and the leading negative phase of a tsunami is a typical recognizable feature of a moderately strong transoceanic tsunami. These results also support previous theory and can help to explain the observed discrepancies.

Key words: 2015 Chilean tsunami, travel time delay, leading negative phase, numerical modeling, corrected long wave, earth's elasticity loading, seawater density stratification, Boussinesq dispersion

Citation: Wang Peitao, Ren Zhiyuan, Sun Lining, Hou Jingming, Wang Zongchen, Yuan Ye, Yu Fujiang. 2021. Observations and modelling of the travel time delay and leading negative phase of the 16 September 2015 Illapel, Chile tsunami. Acta Oceanologica Sinica, 40(11): 11–30, doi: 10.1007/s13131-021-1830-2

1 Introduction

Tsunamis are usually associated with a sudden displacement of the water column due to a number of various trigger mechanisms including earthquakes, submarine or subaerial mass failures (SMFs), volcanism, or atmospheric disturbances (Röbke and Vött, 2017). The tsunami is a type of long wave. In the theory of such waves, the vertical acceleration of water particles is negligible compared to the gravitational acceleration except for the oceanic propagation of tsunamis (Kajiura, 1963). Therefore, it is reasonable to use non-dispersive shallow water equations to simulate tsunami propagation and inundation, especially in the near field within the framework of incompressible fluid theory. Several well-known tsunami models have been developed over a rigid-body earth under the nonlinear shallow water (NLSW) approximation due to the familiarity of the NLSW equations. These models include Australian National University (ANU) and Geoscience Australia (GA) tsunami model, which was called ANUGA (Jakeman et al., 2010; Roberts et al., 2008, 2015); a variant of clawpack

Foundation item: The National Key Research and Development Program of China under contract Nos 2018YFC1407000 and 2016YFC1401500; the National Natural Science Foundation of China under contract Nos 41806045 and 51579090.
*Corresponding author, E-mail: wpt@nmefc.cn

for geophysical flows (GeoClaw), which was developed at the University of Washington (Berger et al., 2011); method of splitting tsunami (MOST) model, developed at the University of Southern California (Titov and Synolakis, 1998); Cornell multigrid coupled tsunami (COMCOT) model, developed at Cornell University (Wang and Liu, 2011); and real-time forecast of tsunamis (RIFT) model, developed at the Pacific Tsunami Warning Center (PTWC) (Wang et al., 2012). Most of these models have been successfully applied to simulate the maximum amplitude or inundation of several recent tsunami events (Tang et al., 2016; Wang et al., 2016; Shan et al., 2017). This type of model has also become the standard tool for quickly providing numerical results for tsunami early warning and hazard assessment since these efforts are currently focusing only on tsunami maximum amplitude and arrival time.

It was not until recently that research revealed the general existence of systematic discrepancies in both the arrival time and initial phase polarity of tsunamis, which has been discovered by comparing observations with predictions based on the shallow water equations of tsunami propagation in the deep ocean. For instance, two bottom pressure gauges and five tidal stations recorded tsunami waveforms with 10–17 min delays relative to the prediction by long wave simulations of the 2004 Sumatra earthquake (M_w 9.1) (Rabinovich et al., 2011, 2017; Prastowo et al., 2018). Rabinovich and Thomson (2007) found that the first wave at all Thai stations was negative during the 2004 Sumatra tsunami. Wei et al. (2008) also noted that an approximate 12-min delay of the tsunami waveform was recorded by three Deep-ocean Assessment and Reporting of Tsunami (DART) stations in the Pacific Ocean after the 2007 Peru earthquake (M_w 8.0). From the figure presented in that study, we can clearly see a negative phase appearing before the main elevated water level compared to their simulated results. The 2010 Chilean tsunami observations in the deep ocean, such as DART buoy stations on the deep ocean floor, tsunami sensors attached to deep ocean bottom cables, and global postioning system (GPS) buoys that monitor sea surface oscillation, have provided evidence that the tsunami delay was up to 30 min (Watada, 2013; Watada et al., 2014; Kato et al., 2011). In addition to the tsunami delay, the leading negative phase (LNP) of the 2010 Chilean tsunami has been widely reported by a large number of researchers (Rabinovich et al., 2013b; Allgeyer and Cummins, 2014; Watada et al., 2014; Eblé et al., 2015; Zaytsev et al., 2016). The LNP for a tsunami has become an increasingly important issue since this event. After the 2011 Tohoku earthquake, a destructive tsunami spread throughout the entire Pacific Ocean and was recorded by numerous offshore bottom pressure stations and approximately 300 coastal tide gauges. Lu et al. (2013) and Prastowo et al. (2018) compared estimated travel times with field records, discovering that, numerically speaking, tsunamis travel 2% faster in the Pacific Ocean Basin. Zaytsev et al. (2017) mentioned that a noteworthy characteristic of three distant DART station records was the presence of a small negative sea-level subsidence preceding the leading frontal crest wave. Similar features were also recognized in the subsequent records of extremely large tsunamis (Eblé et al., 2015; Zaytsev et al., 2016; Heidarzadeh et al., 2018). These studies agree that the systematic discrepancies are more significant at distant stations. The aforementioned findings are also prompting researchers to form a consensus regarding the common occurrence of systematic discrepancies during the long-distance propagation of tsunamis in the deep ocean.

In the past, travel time delay and LNP were mainly attributed to inaccurate bathymetry data, source location errors, numerical truncation, and deviations from the long-wave assumption (Wei et al., 2008; Baba et al., 2009; Kirby et al., 2013). Improvement efforts, however, have only accounted for a small part of the reason for the discrepancies and thus have yet to achieve significant corrections (An and Liu, 2016; Baba et al., 2015; Poupardin et al., 2018; Yamazaki et al., 2011). In recent years, a number of studies have focused on some secondary physical effects, which were typically neglected under the framework of shallow water approximation. Watada (2013) and Watada et al. (2014) indicated that the travel time delay can be explained by considering the effects of density stratification, elastic loading and gravitational potential change. These studies also demonstrated that elastic loading and gravitational potential change associated with the tsunami motion can reproduce the LNP. Tsai et al. (2013) presented a new derivation for the effect of solid Earth elasticity and ocean water compressibility on tsunami wave speeds, showing that these two effects can help to explain timing discrepancies. Inazu and Saito (2013) proposed a simple parameterization of the loading deformation of the seafloor and incorporated it into the shallow water equations to account for the effect of pressure loading on tsunami propagation. Their results demonstrated that this parameterization can correct travel times and waveforms of near-field and far-field tsunamis. This method is computationally efficient and can be easily adopted in tsunami codes with minimal modification. To achieve the best fit, however, the optimal values of the empirical parameters vary somewhat among different prediction stations. Wang (2015) introduced a simple ocean depth-correction in the shallow water model to reduce the discrepancies of the simulated and observed tsunami arrival times by mimicking the effects of compressibility. His method is simple and easy to implement and does not require modification of the governing equations. This approach can account for most of the travel time delay discrepancy. A number of studies have utilized potential theory to evaluate the effects of compressibility, elasticity and gravity on tsunami phase speed by deriving the theoretical solutions of the dispersion relationship (Abdolali and Kirby, 2017; Abdolali et al., 2019; An and Liu, 2016). In addition, Allgeyer and Cummins (2014) developed a corrected tsunami propagation model that included the elastic loading effects of the seafloor by the tsunami as well as the linear density profile. They pointed out that the loading and stratification effects can correct the time delay and reduce the misfitting of tsunami waveforms recorded at large distances. However, their model does not consider the effect of gravitational potential change, Subsequently, Baba et al. (2017) merged the modules developed by Allgeyer and Cummins (2014) with JAGURS code that included the gravitational potential change. Their results revealed that the systematic discrepancies were progressively improved as each of these effects was included.

In this study, we examined the observations of the travel time delay and LNP to demonstrate that systematic discrepancies are also easily identified from the far-field station records of moderate transoceanic tsunamis. The wave characteristics of the LNP and its Pacific-wide distribution are also presented. The main focus of this investigation was to quantitatively evaluate the contribution of coupled secondary physical effects to the systematic discrepancies using the corrected shallow water model incorporating the effects of the self-attraction and loading (SAL) of the earth, seawater density stratification due to compressibility, and Boussinesq dispersion. In addition, we utilized the corrected model to evaluate the impacts of each physical effect on estimated travel time delay and amplitude.

2 Data and methods

2.1 *Tsunami source*

On 16 September 2015, at 22:54:32 UTC, a great earthquake with a moment magnitude (M_w) of 8.3 occurred 22.4 km below the ocean floor on the interface between the Nazca and South American plates in central Chile. According to the US Geological Survey (USGS), the epicenter of the earthquake was located at 31.573°S, 72.674°W, 48 km west of Illapel. At the epicenter of this event, the Nazca plate is moving to the east-northeast at a shallow angle, with a convergence rate of 68–74 mm/a with respect to South America (Barazangi and Isacks, 1976; DeMets et al., 1994; Vigny et al., 2009). The USGS W-phase solution provided a scaler seismic moment of 3.19×10^{21} Nm (M_w 8.3). Its focal mechanism solution was strike: 353°, dip: 19°, rake: 83°, indicating thrust-type faulting with its strike parallel to the trench (Fig. 1a). Even though the majority of the slip was concentrated offshore (Heidarzadeh et al., 2016; Ye et al., 2016), the earthquake still resulted in at least 15 deaths (Li and Ghosh, 2016).

The USGS finite fault solution was used in this study, which is inferred from broadband seismological waveforms using an inverse algorithm (Ji et al., 2002). The finite fault solution with heterogeneous slip distribution can provide more realistic and precise seismic representations than the homogeneous fault. It has been verified that the slip distribution provides essential contributions to tsunami wave characteristics such as wave period, arrival time, inundation, and run-up pattern along the coast (Yamazaki et al., 2013; Wang et al., 2016). The solution consisted of 450 sub-faults, each with an area of 12 km × 8.8 km for a total of 47 520 km^2. The maximum slip according to the solution was approximately 8 m. The tsunami source was assumed to be a combination of 12 km × 8.8 km sub-faults along the fault plane. The vertical crustal displacement of each fault segment was computed using the crustal deformation model of Okada (1985). The sea surface displacement converted from the ocean bottom displacements was used to initialize the tsunami model. As shown in Fig. 1b, the uplift of the vertical displacement was mainly concentrated in the offshore areas near the trench axis and most of the subsidence occurred in onshore coastal zones. Figure 1b shows that the sea surface displacement varied from –0.4 m to 2.4 m.

2.2 *Observation data of the 2015 Chilean tsunami*

The post-tsunami survey data and measured tsunami height indicate that the 2015 Illapel earthquake generated a moderate trans-Pacific tsunami (Aránguiz et al., 2016; Contreras-López et al., 2016). The run-up heights were in the range of 3–6 m, with maximum values of 10–14 m on the near-field coast reported by Contreras-López et al. (2016). The tsunami run-up heights were up to 4 m on the coast concentrated between 29°S and 34°S, and smaller farther south and north (Satake and Heidarzadeh, 2017). Tsunami waves were instrumentally recorded by all of the tide gauges along the Chilean coast and by dozens of Pacific coast tide stations. The tide gauge tsunami amplitudes varied from 1 m to 2 m at the coastal gauges. The maximum tsunami amplitude was 4.7 m at the Coquimbo tide gauge station. In addition, the tsunami was also recorded widely in the deep ocean by DART

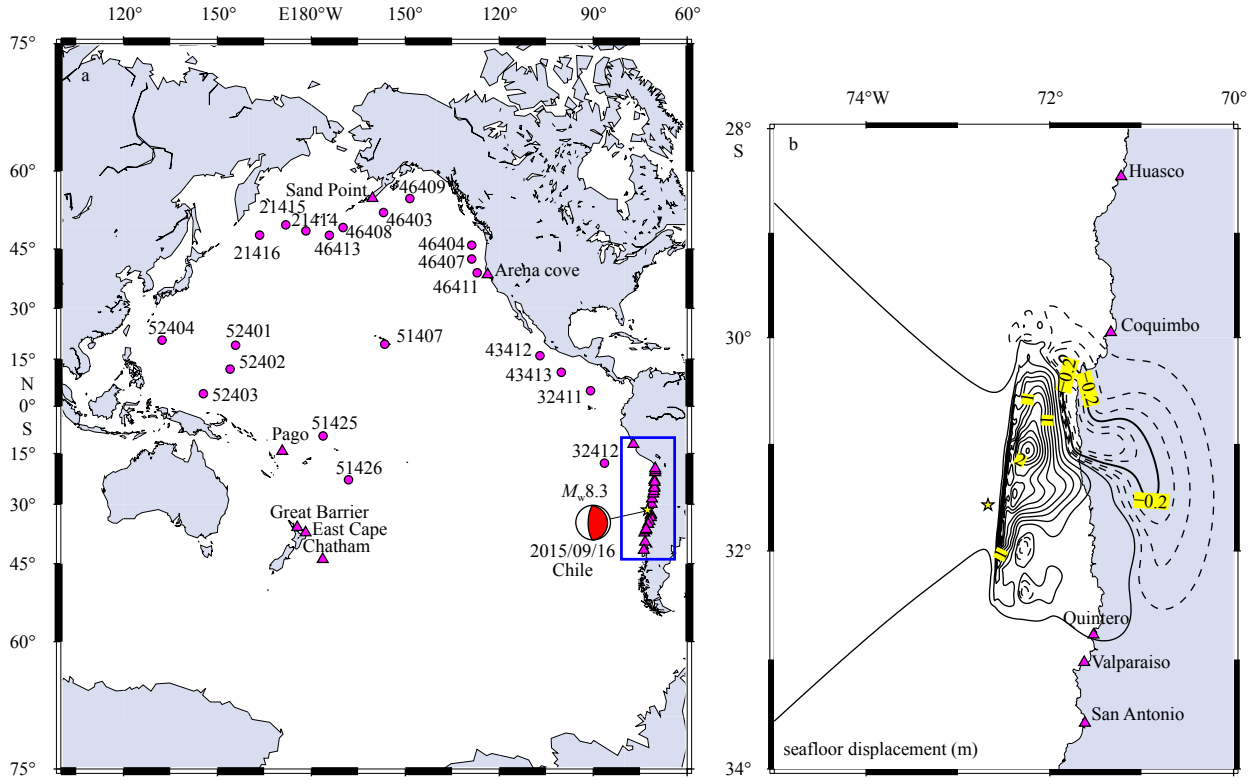

Fig. 1. General map of calculation region showing the locations of 50 selected observatories used in this study and the distribution of seafloor vertical deformation generated by the 2015 M_w 8.3 Illapel earthquake. a. Yellow star represents the epicenter. Solid circles and triangles indicate the locations of DART stations and tide gauges respectively. Detailed information of near-field tide gauges in the rectangular box was listed in Table 1. b. The seafloor vertical displacement was based on US Geological Survey finite fault source model. Black solid lines show the uplift contours with 0.2-m intervals while dashed lines show subsidence contours with 0.05-m intervals.

buoys. The high-quality measurements of the 2015 Chilean tsunami enabled us to examine the main physical attributes of the tsunami waves and to validate the modeling results.

The data used in this study included 21 DART records from the Pacific Ocean provided by the US National Oceanic and Atmospheric Administration (NOAA) and measurements of 22 tide gauges along the Chilean coast provided by Servicio Hidrográfico y Oceanográfico de la Armada de Chile (SHOA), as well as 7 gauges distributed in far-field locations provided by the Directorate of Hydrography and Navigation (DHN), Land Information New Zealand (LINZ) and NOAA's National Ocean Service (NOS/NOAA). The observation stations were selected to provide good coverage of distance and azimuth. As shown in Fig. 1a, the solid circles and triangles, respectively, indicate the locations of the DART stations and tide gauges across the Pacific Ocean. The detailed station information is summarized in Tables 1, 2, and 3. The DART buoys are located at water depths of 3.1–5.9 km. The distance of every DART station to the epicenter ranged from 2 000 km to 17 300 km. The angles of the selected stations in relation to the fault strike varied from 6° to 176°. The DART datasets had varying sampling intervals of 15 s, 1 min, and 15 min. The DART system can transmit 15-s data for several minutes and then switches transmissions to 1-min averages until what is known as the "event mode" terminates (Rabinovich et al., 2013a). In this study, we used the event-mode data, which was transmitted after the start of the event in real-time for several hours at pre-defined 1-min intervals. The sampling interval for all of the tidal gauge data was also 1 min. The event-mode DART data and 1-min sampling interval tide gauge data are suitable for estimating tsunami wave statistical parameters (Zaytsev et al., 2016), such as the arrival time and LNP.

In this study, the following methods were employed to detect the tsunami signal from the sea level records. First, the original time series were de-tided by removing predicted tides using polynomial fittings. The residual time series were used to construct plots of tsunami record for various sites. Next, to suppress residual low-frequency oscillations and to estimate the statistical characteristics of the tsunami waves, the Butterworth IIR high-pass digital filter with a 2-h cutoff period was chosen to filter the datasets. This data processing procedure can avoid introducing a spurious LNP into the original data, something that is usually generated by direct digital filtering. The signal-to-noise ratio of the tsunami signal was greater than 12 (Table 1). A high signal-to-noise ratio makes discernment of the LNP easier. The first 4 h of the tsunami wave data were extracted to estimate the dominating tsunami periods using Fourier analysis.

2.3 *Tsunami modeling*

To accurately calculate the LNP and tsunami arrival time, and to quantitatively evaluate the contribution of the secondary physical effects to the systematic discrepancies improvement, we conducted a tsunami numerical simulation using an improved shallow water equation model known as JAGURS (Baba et al., 2017). The code solves the two-dimensional linear or nonlinear shallow water equations with the effects of elasticity loading, seawater density stratification, and Boussinesq dispersion. In this study, we focused on the comparative analysis of the simulated 2015 Chilean tsunami LNP and travel time delays with deep-ocean records. The calculation region was set as 75°S–70°N and 100°E–60°W to cover the Pacific Ocean Basin with a grid step of 4 arc min (Fig. 1a). The 4-arc min grid was resampled from the 30-arc sec GEBCO-2014 bathymetric data. The linear simulations with a time step of 5.0 s were conducted to meet the Courant-Friedrichs-Lewy (CFL) numerical stability criterion and a Manning coefficient of 0.025 was considered to account for the bottom friction effects. The total simulation time reached 30 h.

The JAGURS code was improved following the method proposed by Allgeyer and Cummins (2014). The model was made more suitable for the simulation of far-field tsunamis by taking into account the seawater density stratification, elastic loading effects, and Boussinesq term. They replaced the original continuity equation with a derived equation by introducing the displacement at the seafloor from its depth H and assuming that the seawater density varies linearly with ocean depth. Previous researches did not include the gravitational potential change effect. In the upgraded JAGURS code the gravitational potential change has been taken into account. The vertical deformation of the seafloor due to elastic loading and gravitational potential change (often referred to as the ocean self-attraction and loading effect, or SAL) can be expressed in the form of a Green's function. The revised governing equations for JAGURS with the dispersion term are expressed as follows.

$$\rho_H \frac{\partial(\eta+\xi)}{\partial t} = -\frac{\rho_{\text{ave}}}{R\sin\theta}\left[\left(\frac{\partial M}{\partial\varphi}+\frac{\partial(N\sin\theta)}{\partial\theta}\right)\right], \tag{1}$$

$$\begin{aligned}\frac{\partial M}{\partial t}+\frac{1}{R\sin\theta}\frac{\partial}{\partial\varphi}\left(\frac{M^2}{H+\eta}\right)+\frac{1}{R}\frac{\partial}{\partial\theta}\left(\frac{MN}{H+\eta}\right)=\\ -\frac{g(H+\eta)}{R\sin\theta}\frac{\partial h}{\partial\varphi}-fN-\frac{gn^2}{(H+\eta)^{7/3}}M\sqrt{M^2+N^2}+\\ \frac{H^2}{3R\sin\theta}\frac{\partial}{\partial\varphi}\left[\frac{1}{R\sin\theta}\left(\frac{\partial^2 M}{\partial\varphi\partial t}+\frac{\partial^2(N\sin\theta)}{\partial\theta\partial t}\right)\right],\end{aligned} \tag{2}$$

$$\begin{aligned}\frac{\partial N}{\partial t}+\frac{1}{R\sin\theta}\frac{\partial}{\partial\varphi}\left(\frac{MN}{H+\eta}\right)+\frac{1}{R}\frac{\partial}{\partial\theta}\left(\frac{N^2}{H+\eta}\right)=\\ -\frac{g(H+\eta)}{R}\frac{\partial h}{\partial\theta}+fM-\frac{gn^2}{(H+\eta)^{7/3}}N\sqrt{M^2+N^2}+\\ \frac{H^2}{3R}\frac{\partial}{\partial\theta}\left[\frac{1}{R\sin\theta}\left(\frac{\partial^2 M}{\partial\varphi\partial t}+\frac{\partial^2(N\sin\theta)}{\partial\theta\partial t}\right)\right].\end{aligned} \tag{3}$$

Equation (1) is the continuity equation derived by Allgeyer and Cummins (2014). Equations (2) and (3) are the equations of motion for the nonlinear shallow water equation with Boussinesq terms. Here, ξ is the displacement at the seafloor from its depth H; ρ_H and ρ_{ave} are the seawater density at the seafloor and the average along the vertical profile, respectively; M and N denote the depth-integrated flow along the φ (longitudinal) and θ (latitudinal) directions, respectively; R is the earth's radius; t is time; η is the water height from the sea surface at rest; g is the gravitational acceleration; f is the Coriolis parameter; and n is Manning's roughness coefficient.

The vertical displacement of the seafloor relative to the geoid was calculated by superimposing a Green's function, as follows:

$$G(r',r)=G_{\text{SAL}}(\alpha)=\frac{-R}{M_{\text{e}}}\sum_{n=0}^{\infty}(1+k_n^{'}-h_n^{'})P_n(\cos\alpha), \tag{4}$$

where r denotes any position on the earth's surface, with the point mass is located at r'; M_{e} is the mass of the earth; α is the angular distance between r' and r; $k_n^{'}$ and $h_n^{'}$ are the loading love number of angular order n; and P_n refers to the n-th Legendre polynomial.

Table 1. DART stations and tide gauges that recorded the leading negative phase during the 2015 Illapel, Chile tsunami

No.	Station	Location (DART) / Institution or country (tide gauges)	Coordinates		Sampling interval/min	SNR[3)]/dB
			Latitude	Longitude		
1	21414	184 n mile[1)] SW of Adak, Alaska, USA	48.948°N	178.247°E	1[2)]	20
2	21415	175 n mile South of Attu, Alaska, USA	50.183°N	171.847°E	1	23
3	21416	240 n mile SE of Kamchatka Peninsula, Russia	48.040°N	163.490°E	1	21
4	32411	710 n mile WSW of Panama City, Panama	4.995°N	90.850°W	1	15
5	32412	630 n mile SW of Lima, Peru	17.979°S	86.369°W	1	33
6	43412	240 n mile SW of Manzanillo, Mexico	16.026°N	106.997°W	1	20
7	43413	360 n mile SSW of Acapulco, Mexico	10.842°N	100.137°W	1	21
8	46403	230 n mile SE of Shumagin Island, Alaska, USA	52.650°N	156.946°W	1	23
9	46404	230 n mile West of Astoria, Oregon, USA	45.853°N	128.775°W	1	18
10	46407	210 n mile West of Coos Bay, Oregon, USA	42.665°N	128.806°W	1	16
11	46408	212 n mile South of Umnak Island, Alaska, USA	49.668°N	169.888°W	1	23
12	46409	240 n mile SE of Kodiak, Alaska, USA	55.300°N	148.515°W	1	24
13	46411	150 n mile West of Mendocino Bay, California, USA	39.342°N	127.021°W	1	19
14	46413	243 n mile SSE of Adak, Alaska, USA	47.999°N	174.227°W	1	25
15	51407	140 n mile SE of Honolulu, Hawaii, USA	19.553°N	156.546°W	1	21
16	51425	370 n mile NW of Apia, Samoa	9.510°S	176.241°W	1	27
17	51426	400 n mile SE of Kingdom of Tonga	22.974°S	168.139°W	1	26
18	52401	610 n mile ENE of Saipan, Northern Mariana Islands	19.261°N	155.754°E	1	22
19	52402	540 n mile ESE of Saipan, Northern Mariana Islands	11.869°N	154.039°E	1	18
20	52403	345 n mile North of Manus Island, PNG	4.020°N	145.520°E	1	17
21	52404	760 n mile NE of Manila, Philippines	20.790°N	132.340°E	1	19
22	Coquimbo	SHOA, Chile	29.950°S	71.335°W	1	39
23	Quintero	SHOA, Chile	32.775°S	71.525°W	1	33
24	Valparaiso	SHOA, Chile	33.027°S	71.626°W	1	30
25	Huasco	SHOA, Chile	28.461°S	71.224°W	1	28
26	San Antonio	SHOA, Chile	33.582°S	71.618°W	1	29
27	Caldera	SHOA, Chile	27.065°S	70.825°W	1	28
28	Bucalemu	SHOA, Chile	34.639°S	72.046°W	1	26
29	Paposo	SHOA, Chile	25.009°S	70.469°W	1	16
30	Constitucion	SHOA, Chile	35.356°S	72.458°W	1	23
31	Chanaral	SHOA, Chile	26.352°S	70.634°W	1	25
32	Taltal	SHOA, Chile	25.408°S	70.492°W	1	18
33	Lebu	SHOA, Chile	37.594°S	73.664°W	1	20
34	Coronel	SHOA, Chile	37.029°S	73.152°W	1	21
35	Quiriquina	SHOA, Chile	36.636°S	73.057°W	1	22
36	Talcahuano	SHOA, Chile	36.701°S	73.106°W	1	23
37	Mejillones	SHOA, Chile	23.098°S	70.451°W	1	17
38	Antofagasta	SHOA, Chile	23.653°S	70.404°W	1	21
39	Patache	SHOA, Chile	20.803°S	70.198°W	1	16
40	Corral	SHOA, Chile	39.887°S	73.427°W	1	18
41	Iquique	SHOA, Chile	20.205°S	70.148°W	1	15
42	Pisagua	SHOA, Chile	19.596°S	70.216°W	1	14
43	Ancud	SHOA, Chile	41.867°S	73.833°W	1	14
44	Callao	DHN, Peru	12.069°S	77.167°W	1	15
45	Chatham	LINZ, New Zealand	44.025°S	176.369°W	1	15
46	East Cape	LINZ, New Zealand	37.550°S	178.159°E	1	18
47	Arena cove	NOS/NOAA, USA	38.913°N	123.705°W	1	18
48	Pago	NOS/NOAA, USA	14.277°S	170.691°E	1	23
49	Great Barrier	LINZ, New Zealand	36.189°S	175.489°E	1	20
50	Sand Point	NOS/NOAA, USA	55.337°N	160.502°W	1	12

Note: [1)] 1 n mile = 1.852 km. [2)] "Event-mode" DART data. [3)] $\mathrm{SNR} = 20\log_{10}\left(\frac{A_{\mathrm{signal}}}{A_{\mathrm{noise}}}\right)$, A_{signal}: maximum amplitude of signal, A_{noise}: maximum amplitude of Noise. PNG: Papua New Guinea, SHOA: Servicio Hidrográfico y Oceanográfico de la Armada de Chile, LINZ: Land Information New Zealand, NOS/NOAA: National Oceanic and Atmospheric Administration's National Ocean Service.

The above governing equations were solved by a finite difference method implementation using a staggered grid scheme. For a more detailed description, please refer to Baba et al. (2015, 2016, 2017).

Table 2. Statistical characteristics of the 2015 Illapel, Chile tsunami estimated from DART Buoy records and tide gauge data

Station	Distance[1)]/km	Azimuth[2)]/(°)	LNP			First frontal crest wave	Max. wave			Peak periods /min	$\lvert\zeta_1/\zeta_2\rvert$ /%
			$T^{3)}$/h	$\zeta_1^{4)}$/cm	$\tau^{5)}$/min	$\zeta_2^{6)}$/cm	$\zeta_3^{7)}$/cm	Sign	No. of the max. wave		
32412	2 044	39	1.85	−0.79	54	6.82	6.82	(+)	1	75, 40, 14	12
32411	4 499	22	5.80	−0.82	24	1.82	1.82	(+)	1	75, 28, 9	45
43413	5 549	30	7.29	−0.62	30	1.41	2.22	(−)	3	44, 28, 6	44
43412	6 435	33	8.34	−0.62	52	2.02	2.66	(+)	2	41, 18, 9	30
51426	9 178	105	12.22	−0.44	16	1.36	2.73	(−)	4	87, 38, 17	32
46411	9 674	32	13.44	−0.56	27	1.39	1.39	(+)	1	44, 28, 17	40
46407	10 042	31	14.00	−0.54	28	1.32	1.32	(+)	1	50, 29, 17	41
46404	10 291	29	14.61	−0.47	28	1.09	1.09	(+)	1	71, 31, 17	43
51407	10 577	64	14.00	−0.61	31	1.86	1.86	(+)	1	62, 18	33
51425	10 712	99	14.21	−0.44	32	0.72	4.25	(−)	2	62, 33, 18	61
46409	12 026	29	16.49	−0.47	36	2.05	2.05	(+)	1	71, 38, 13	23
46403	12 384	34	16.67	−0.57	30	2.04	2.04	(+)	1	62, 33, 15	28
46408	13 111	40	17.34	−0.57	24	2.14	2.14	(+)	1	31, 18, 13	27
46413	13 365	43	17.12	−0.37	47	1.89	2.59	(−)	2	62, 41, 13	20
21414	13 928	43	18.05	−0.54	31	1.37	1.99	(−)	2	66, 31, 15	39
21415	14 404	42	18.63	−0.47	34	1.69	2.42	(+)	3	66, 31, 13	28
52402	14 764	97	19.67	−0.42	52	0.91	1.63	(−)	2	81, 33, 14	46
52403	14 987	113	21.39	−0.33	28	0.33	1.16	(+)	4	33, 15	100
52401	15 003	87	18.60	−0.22	48	1.46	1.46	(+)	1	66, 44, 14	15
21416	15 504	45	18.95	−0.52	49	0.92	2.17	(+)	5	66, 44, 17	57
52404	17 253	103	22.59	−0.81	65	1.28	1.99	(−)	2	81, 31, 15	41
Quintero	172	148	0	−8.14	18	136	181	(+)	2	31, 14	6
Valparaiso	189	156	0	−9.83	23	117	173	(+)	3	35	8
Coquimbo	221	42	0	−24.18	21	93	466	(+)	4	33, 17	26
San Antonio	244	163	0	−6.60	30	65	108	(−)	4	47, 18	10
Bucalemu	345	176	0	−4.62	40	45	85	(−)	8	38, 18	10
Huasco	373	29	0	−3.75	27	47	80	(+)	5	31, 13	8
Constitucion	421	176	0	−4.37	50	50	110	(+)	3	62, 44, 18	9
Caldera	532	27	0.20	−4.26	34	34	90	(+)	10	31, 15	13
Quiriquina	563	170	0.77	−5.48	34	24	78	(−)	3	87, 27, 8	23
Talcahuano	571	169	0.60	−7.65	54	43	115	(−)	3	87, 31, 17	18
Coronel	608	169	0.60	−5.61	42	25	62	(+)	5	115, 44	22
Chanaral	613	26	0.40	−4.45	24	42	119	(+)	3	31	11
Lebu	675	166	0.38	−3.03	45	22	32	(+)	3	44, 15	14
Taltal	717	25	0.47	−3.37	26	20	33	(+)	6	31, 18, 9	17
Paposo	761	24	0.32	−2.95	36	19	19	(+)	1	66, 44, 33, 17	16
Antofagasta	908	22	0.70	−2.41	24	18	46	(−)	4	44	13
Corral	927	169	1.20	−3.47	47	24	32	(+)	4	87, 33	14
Mejillones	967	21	0.80	−3.44	24	14	29	(−)	2	41, 25, 17	25
Ancud	1 149	168	1.63	−3.74	48	6	16	(−)	4	71, 18	62
Patache	1 223	19	1.10	−3.72	30	12	33	(−)	2	47	31
Iquique	1 289	19	0.80	−4.21	48	11	29	(+)	7	44, 25, 15	38
Pisagua	1 354	18	0.97	−2.78	50	10	20	(+)	7	47, 13	27
Callao	2 217	6	2.88	−6.21	30	19	59	(+)	9	47, 31, 13	32
Chatham	8 601	127	12.35	−8.14	24	29	48	(+)	4	76, 35, 19	28
East Cape	9 385	124	12.85	−0.97	26	8	14	(−)	5	20	12
Arena Cove	9 445	30	13.48	−1.23	24	6	10	(−)	6	81, 33, 15	21
Great Barrier	9 666	124	13.62	−2.06	24	12	20	(+)	5	38, 15	17
Pago	11 557	110	13.73	−4.87	12	13	47	(+)	5	18, 9	37
Sand Point	12 713	35	18.17	−2.15	28	9	19	(+)	8	41, 25, 16	24
Average					33					72, 30, 18	40

Notes: [1)] The distance of every station to the epicenter based on spherical earth system. [2)] The angles of the station in relation to fault strike. [3)] Travel time of the LNP is in hours after the earthquake. [4)] The maximum amplitude of the LNP. [5)] The duration of the LNP. [6)] The maximum amplitude of the first frontal crest wave. The first frontal crest wave usually is defined as the crest of the first tsunami wave. In general, it is the max over the first zero-crossing wave period since tsunami arrived. [7)] The maximum tsunami amplitude records.

Table 3. Summary of the observed travel time and the travel time delays for the 2015 Chilean tsunamis at DART buoy stations

Station	Distance[1)]/km	Depth/m	T_c[2)]/h	T_d[3)]/min	Corrections of the travel time delay/min			
					SAL	Density stratification	Wave dispersion	ECD[4)]
32412	2 044	4 320	2.87	4.5	4.3	3.8	3.5	2.3
32411	4 499	3 229	6.58	3.6	2.6	1.8	2.1	0.0
43413	5 549	3 740	7.89	3.9	2.8	1.8	2.5	–0.7[5)]
43412	6 435	3 142	9.32	5.1	3.3	2.0	3.5	–0.7[5)]
51426	9 178	5 659	12.61	11.4	9.0	7.6	10.7	4.1
46411	9 674	4 325	14.00	9.5	7.6	5.7	7.8	1.8
46407	10 042	3 300	14.59	8.4	6.1	4.5	6.7	0.0
46404	10 291	3 738	15.17	8.3	6.2	4.3	6.6	0.0
51407	10 577	4 737	14.64	12.5	10.4	8.2	10.6	3.8
51425	10 712	4 889	14.87	13.7	11.1	9.4	12.4	5.0
46409	12 026	4 194	17.24	10.3	7.7	5.4	8.3	0.0
46403	12 384	4 513	17.31	11.9	9.3	7.1	10.2	1.7
46408	13 111	5 372	17.87	13.2	9.9	7.6	11.4	1.9
46413	13 365	5 583	18.04	14.4	11.7	8.8	12.5	3.1
21414	13 928	5 479	18.68	14.4	11.6	8.6	12.5	2.7
21415	14 404	4 855	19.33	18.0	15.0	12.0	16.4	6.2
52402	14 764	5 886	20.71	21.3	17.6	15.3	18.2	8.2
52403	14 987	4 466	21.92	20.9	17.7	14.5	17.6	7.7
52401	15 003	5 570	20.62	18.6	16.0	12.8	18.0	5.4
21416	15 504	5 831	19.88	15.5	12.4	9.3	13.4	2.6
52404	17 253	5 864	23.96	21.9	17.8	14.9	18.2	6.3
Average contribution rate					21%	39%	18%	78%

Note: [1)] The distance of every station to the epicenter based on spherical earth system. [2)] T_c indicates travel time of the first frontal crest wave is in hours after the earthquake. [3)] T_d indicates travel time of the first frontal crest wave delay relative to linear long waves is in minutes. [4)] Improved corrections with self-attraction and loading due to elasticity loading, seawater density stratification due to compressibility and dispersion effects. [5)] Negative value represent the first frontal crest wave arrive earlier than improved phase corrections results.

In this study, we employed the code to carry out five simulation scenarios for the 2015 Chilean tsunami event by considering each secondary physical effect separately. The simulated results were also verified against deep-ocean records and analyzed in term of travel time delay, LNP, and tsunami distribution to evaluate the contribution of each physical effect to the systematic discrepancies improvement.

3 Characteristics of tsunami waves

We used the de-tided tsunami records from various sites to estimate the statistical characteristics. The statistical properties utilized in this study to investigate the 2015 Chilean tsunami were as follows.

(1) Travel time①, duration, and maximum wave amplitude of the leading negative phase;

(2) Maximum wave amplitude of the first frontal crest wave;

(3) Maximum amplitude and its sign (either the elevation or depression wave);

(4) Number of the maximum wave (whichever wave was the largest);

(5) Tsunami peak period and amplitude ratio of the LNP to the first frontal crest wave.

3.1 *General statistical properties*

The summarized statistical characteristics for the tsunami wave are listed in Table 2. Time-series plots for all of the selected stations are presented in Figs 2 and 3. The analysis revealed several important features of the 2015 Chilean tsunami during its propagation in both the near and far fields.

The 2015 Illapel, Chile tsunami waves were clearly recorded across the entire Pacific Ocean Basin. The maximum tsunami wave amplitude of 4.7 m was measured during the fourth wave along the Chilean coast at Coquimbo, located just north of the main rupture area. The adjacent gauges, however, received tsunami wave amplitudes that did not exceed 2 m. Within 1 000 km of the epicenter, the tsunami waves exhibited considerable differences in amplitude, ranging from 4.7 m down to 0.2 m. The tsunami distribution type tends to be determined by the complexity of the local topography, source geometry, and slip distribution. As shown in Fig. 3, clear tsunami signals at all considered DART buoy stations were recorded. The maximum tsunami amplitude, recorded by DART Buoy 32412, was 6.82 cm. The amplitude at the other stations ranged from 1.1 cm to 4.3 cm in the deep-ocean. These finding reveal that it was a typical moderate transoceanic tsunami event causing fluctuations in the Pacific Ocean Basin. The leading elevation amplitude and maximum amplitude of the tsunami wave tend to attenuate with propagation distance. According to Table 2, an important characteristic was that at all of the examined tide gauges, with the exception of Paposo, the maximum wave was not the first wave, but generally occurred several hours later (Fig. 2). This is one of the main reasons that tsunamis often cause disasters in coastal regions. A similar feature could also be found at the DART buoy stations. At all of the stations, a few of the maximum tsunami amplitudes were depressions, which may have then led to higher run-up heights. Hence, effective early warning information considering the aforementioned tsunami threat behaviors can further reduce casualties and property losses in the near-shore zone.

The tsunami waves were first received at the tide gauges closest to the main rupture region within 25 min of the earth-

① Generally, tsunami travel time is defined as the time required for the first tsunami wave to propagate from its source to a given point.

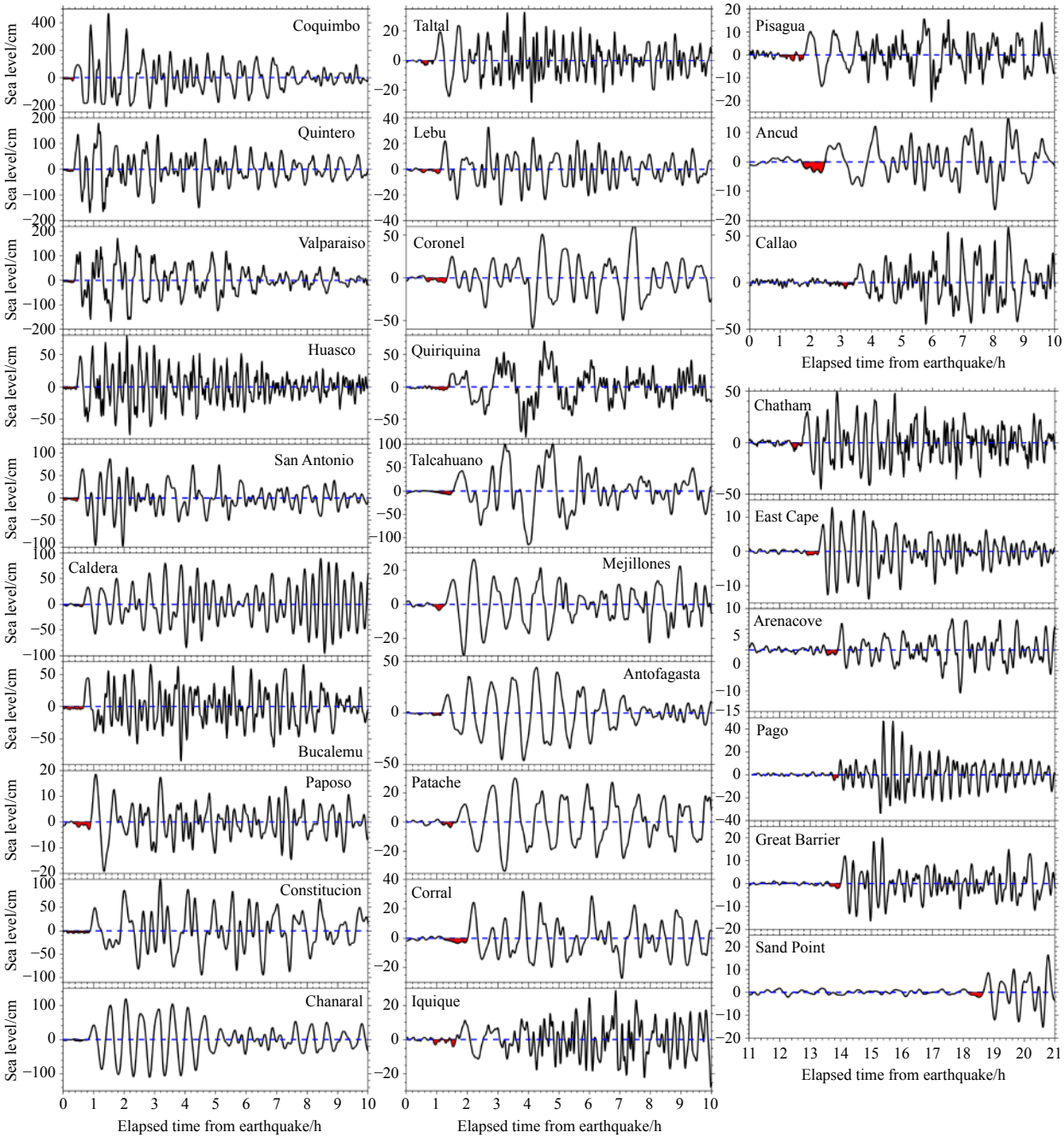

Fig. 2. The 16 September 2015 Chile tsunami recorded by tide gauges at 22 near-field sites and 7 far-field sites. The red shaded areas are the leading negative phase marking the arrival of the tsunami waves.

quake (Table 2, Fig. 2), e.g., Coquimbo, Quintero, Valparaiso, and San Antonio. The tsunami then propagated out into the Pacific Ocean and farther south and north of Chilean coast. The leading wave arrived in Peru after approximately 3 h. The nearest DART buoy, 32412, recorded a sea-level oscillation after 2.5 h. The 2015 Chilean tsunami took 25 h to spread across the entire Pacific Ocean. The travel time versus distance from the epicenter is plotted in Fig. 4, based on the deep-ocean data. As shown in this figure, there was a linear relationship between travel time and propagation distance. The black line is the best fit, with a slope of 740. Note that the slope represents the average phase velocity (740 km/h) of the tsunami wave traveling across the Pacific Ocean Basin.

Column 11 of Table 2 presents the period analysis results. These results illustrate that the tsunami spectral energy was distributed in period bands of 14–18 min, 27–44 min, and 44–75 min for most of the analyzed stations. The tsunami spectrum exhibited multiple peaks due to source geometry and multi-scale bathymetric features. The peak period at approximately 30 min and 15 min for the 2015 Illapel event were possibly the most dominant tsunami source periods, since these two frequency components are the most common in Table 2. There was a significant correlation between the dominant period bands and the angles from the fault strike in both the near and far field. For a station located normal to the fault strike, the peak period was mainly dictated by the width of the tsunami source. Contrary to this, the governing period was possibly influenced by the length of the

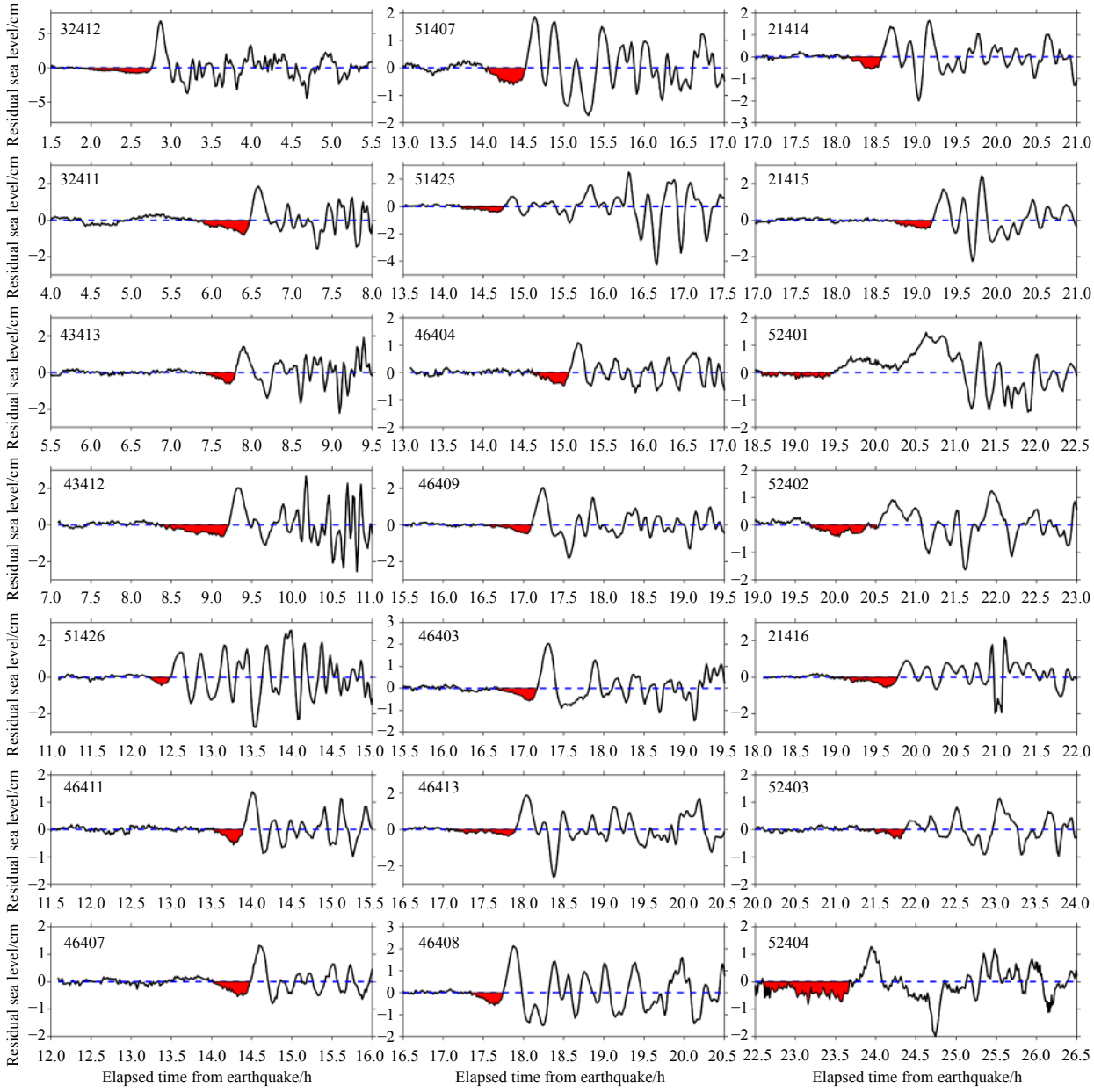

Fig. 3. Tsunami waveform from 2015 Illapel tsunami recorded on DART stations across the Pacific Ocean. The red shaded areas are the leading negative phase that preceded the arrival of the main tsunami.

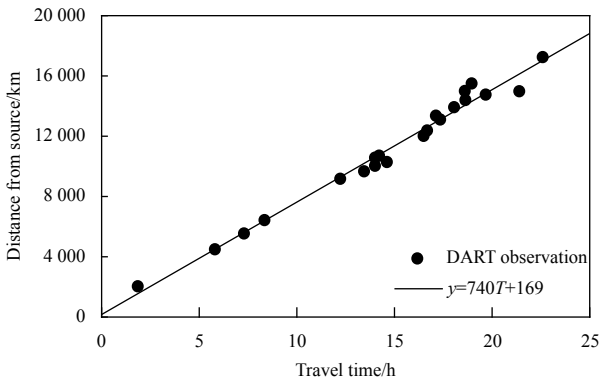

Fig. 4. The relationship between the distance from the source and travel time. The black circles indicate the data available from DART observations for the 2015 Illapel, Chile tsunami.

source if the station was located parallel to the fault strike. Similar results have been reported in previous recent tsunami (Heidarzadeh and Satake, 2013, 2014; Heidarzadeh et al., 2015).

It is known that the main governing periods of tsunamis are normally dictated by the dimensions of the earthquake fault. The spectra of the tide gauge stations are strongly influenced by topographic features. Therefore, we applied the dominant period of the DART data to verify the dimensions of the selected tsunami source. The dimensions of the tsunami source were estimated from the following formulas:

$$L \approx \frac{\lambda_L}{2} = \frac{1}{2} T_L \sqrt{gh}, \tag{5}$$

$$W \approx \frac{\lambda_W}{2} = \frac{1}{2} T_W \sqrt{gh}, \tag{6}$$

where L and W are the length and width of the tsunami source, respectively; λ_L and λ_W represent tsunami wavelengths corresponding to the long and short axis of the tsunami source, respectively; T_L and T_W are the governing periods originated from the source length and width, respectively; and h = 4 700 m is the average water depth of DART buoy stations. The average dominant periods of 33 min and 16 min were substitute into Eqs (5) and (6). The estimated source dimensions, i.e., a length of 212 km in the strike direction and a width of 103 km in the dip direction, agreed with the extent of the major initial deformation distribution, as shown in Fig. 1b.

3.2 *Observed characteristics of leading negative phase*

A typical feature of the 2015 Chile tsunami wave series, as revealed by the analyses of the coastal and open-ocean records near the Chilean coast and across the Pacific Ocean, was the small leading negative phase with long period that preceded the arrival of the first elevated wave (Figs 2 and 3). As described by Rabinovich et al. (2013b), the profile of the leading negative wave was also unusual, consisting of a gradually downward descending concave sea level profile, followed by an abrupt sea level increase. As shown in Figs 2 and 3, it was quite difficult to identify the exact arrival time of the leading negative wave due to the very smooth initial phase and small amplitude relative to the background noise, especially for the tide gauges located near the source area. Rabinovich et al. (2013b) suggested that the possible causes for the LNP may have originated with a negative depression, after they had ruled out the possibility of artificial error during data processing. With respect to the 2015 Chilean event, the profile of the leading negative wave began to form at the time the earthquake occurred at Quintero, Valparaiso, Coquimbo, San Antonio, Bucalemu, Huasco, and Constitucion stations, all of which were located in the subsidence deformation areas. The possible explanation that the initial negative depression of the tsunami sources caused the leading negative wave sounds reasonable for the coastal stations closed to rupture areas. In other words, we expect an initial elevation in the seaward region of subduction zones. However, the LNPs were still recorded by the far-field seaward stations (Figs 2 and 3). Watada et al. (2014) suggested that the far-field LNP is a characteristic response of the self-gravitating elastic Earth to tsunami loading, which causes reverse dispersion of long wave. The LNP can be modeled by considering the solid earth deformation due to elastic loading. According to their theory, if the initial phase at the tsunami source is positive seaward, the initial phase recorded at the far field becomes negative. In contrast, if the initial phase at the source is negative seaward, the initial phase recorded at the far field becomes positive.

Table 2 shows the maximum amplitude and duration of the observed leading negative phase (LNP) at all of the analyzed stations in both the deep-ocean and near-shore. The maximum negative amplitudes of the initial phases ranged from 0.21 cm to 0.82 cm at the DART stations and 0.97 cm to 24.2 cm at the tide gauge sites (the red-shaded areas in Figs 2 and 3). The durations of the LNP (τ) ware approximately 16–54 min at the DARTs and 12–54 min at the tide gauges. The average duration of all the selected stations is 33 min, which is almost equivalent to the main governing period of the tsunami source. The possible effect of source directivity on the duration of the LNP was not obvious due to the sparseness of observations over the Pacific Ocean and the complex bathymetry. The amplitude ratios of the LNP relative to the amplitude of the first frontal crest wave varied from 12% to 100% at the DARTs and 6% to 62% at the tide gauges. The average amplitude ratio reached 40%. These results indicate that the amplitudes of the initial phase were significant compared to the leading elevation amplitudes (Table 2). Based on the statistical features of the LNP summarized in Table 2, we did not find any apparent dependency of the duration, amplitudes, or amplitude ratio on the distance from the source, although the durations and amplitudes of the LNP exhibited obvious dependence on the earthquake magnitude. In this context, two empirical equations were derived for expressing the relationship among the duration, amplitude, and earthquake magnitude (Heidarzadeh et al., 2018).

The contours of the amplitude ratios listed in Table 2 are plotted in Fig. 5 based on the LNP signature feature recorded As shown in Fig. 5, the amplitude ratio intensity nearest the source was weaker than the intensities distributed in the areas far from the epicenter. The amplitude ratios gradually became more pronounced along the propagation direction of the tsunami. Nevertheless, we still could not determine the quantitative dependency of the amplitude ratios on the propagation distances based on the sparseness observational data. The conclusion that the LNP was not a near-source feature, or at least not distinguishable nearest the tsunami source, is supported by the investigations of Watada (2013), Allgeyer and Cummins (2014), Eblé et al. (2015) and Baba et al. (2017). Comparison of the maximum simulated tsunami amplitude (Fig. 6) with Fig. 5, revealed that they exhibited similar spatial distribution, especially in the Southeast Pacific Ocean. Their intensity changes, however, displayed opposite trends. The maximum amplitude was found to decrease with distance from tsunami source. Contrary to this, the LNP amplitude ratios becomes more significant. The amplitude ratios along the tsunami travel paths were significantly enhanced compared to other directions. The most pronounced intensity of the leading negative wave appears along the travel path most perpendicular to the fault strike.

4 Accurate numerical simulation of the 2015 Illapel, Chile tsunami

The typical differences between observations and simulations of characteristics such as arrival time delay and initial negative polarity may confidently be attributed to the inadequate fit between the modeled and observed waveforms obtained from observation instruments to the limited resolution of the bathymetry data, nonlinear effects, Coriolis force, bottom friction, grid size and other factors. The aforementioned effects did not account for the observed systematic differences, especially in the far field. To reduce the systematic discrepancies in both arrival time delay and LNP between the simulations and the calculated synthetic results based on the standard linear shallow water (LSW) equations, the numerical investigations were conducted using the modified LSW equations model, which included the SAL, seawater density stratification due to compressibility, and wave dispersion effects, and then compared with observed DART data. Because we mainly focused on tsunami propagation in the deep ocean, we will not discuss the comparative analysis between tsunami observations and simulations in coastal areas.

4.1 *Reproducible leading negative waves*

The leading negative phase is typically not reproduced by the tsunami models commonly used for forecasting, although it has been well defined in recent events. According to a suggestion by Watada et al. (2014), the leading negative waves can be modeled by considering the solid Earth deformation due to tsunami loading. We compared the results of the three simulation scenarios in

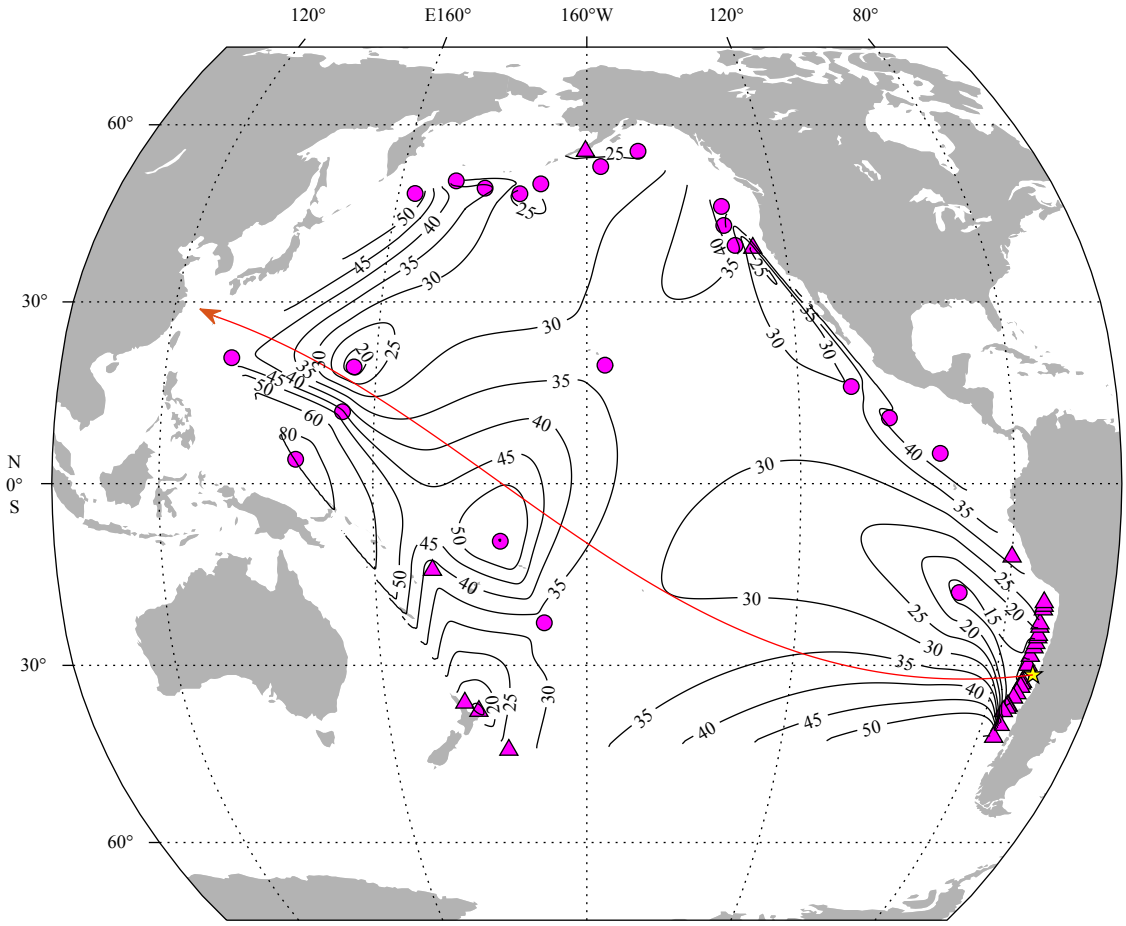

Fig. 5. Contours of the amplitude ratio (%) of the LNP to the first frontal crest wave determined from near-field and far-field records across the Pacific Ocean. The solid line with red arrow represents the normal direction to the fault strike. Yellow star represents the epicenter. Solid circles and triangles indicate the locations of DART stations and tide gauges respectively.

Fig. 7 to the tsunami waveforms recorded by the 21 DART buoys. These three scenarios were composed of the standard LSW simulation results, the LSW simulation results considering the SAL effect, and the LSW results considering the ECD (the combined effects of elasticity loading, density stratification due to compressibility, and dispersion) effect simulations. In most cases, the simulated waveforms were in good agreement with the observations. The exceptions were a few DART Bouys in the western part of the Pacific Ocean, in particular, DART Buoys 52401, 52402, 52403, and 52404. The reason for this disagreement is not quite clear. Figure 7 indicates that the corrected results taking into account the Earth's elasticity effect could reproduce the leading negative phase at most DART stations. However, the LNP in the observed tsunami waveforms was not simulated by the LSW model at all stations. The agreement between the simulated and observed tsunamis was improved further in terms of LNP arrival time and maximum tsunami amplitude by additionally considering the wave dispersion and seawater density stratification based on the LSW equations with SAL. The tsunami waveforms calculated by the LSW equations with wave dispersion and seawater density stratification are compared with tsunami records in Fig. 8. According to the comparison at near-field DART Stas 32411 and 32412 (Fig. 8), the effects of seawater density stratification and wave dispersion were small because of the short travel time. By contrast, at far-field stations, the distinguishing contributions of these effects in the modeled waveforms were evident in travel time delay. The dispersion effect caused the tsunami amplitude to diminish in the leading tsunami waves trains, but enhanced the amplitude of the latter wave trains. From Fig. 8, we conclude that the seawater density stratification effect only reduces the tsunami speed, but does not alter its waveforms. The wave dispersive effect not only changes the tsunami arrive time of the first elevated wave but also distorts the waveforms. However, the correction scheme that considers the wave dispersion and seawater density stratification respectively cannot simulate the leading negative phase. Similar conclusions can also be found in previous studies (Tsai et al., 2013; Watada, 2013; Allgeyer and Cummins, 2014). Nevertheless, the coupling of all these effects does not perfectly replicate the leading negative waves, which may be due to model initialization errors, as well as other unknown reasons. According to the analysis by Allgeyer and Cummins (2014), the extent of tsunami waveform distortion caused by the loading and density stratification effects will depend on the characteristics of the source (e.g., the wavelength), as well as the particular ocean path traversed from source to receiver.

In addition to the LNP, there was a 2–22 min difference in arrival time between the observations and simulations. The simulated results from the LSW with SAL and the LSW with ECD significantly reduced the time deviation. A detailed discussion about travel time delay is presented in the next section.

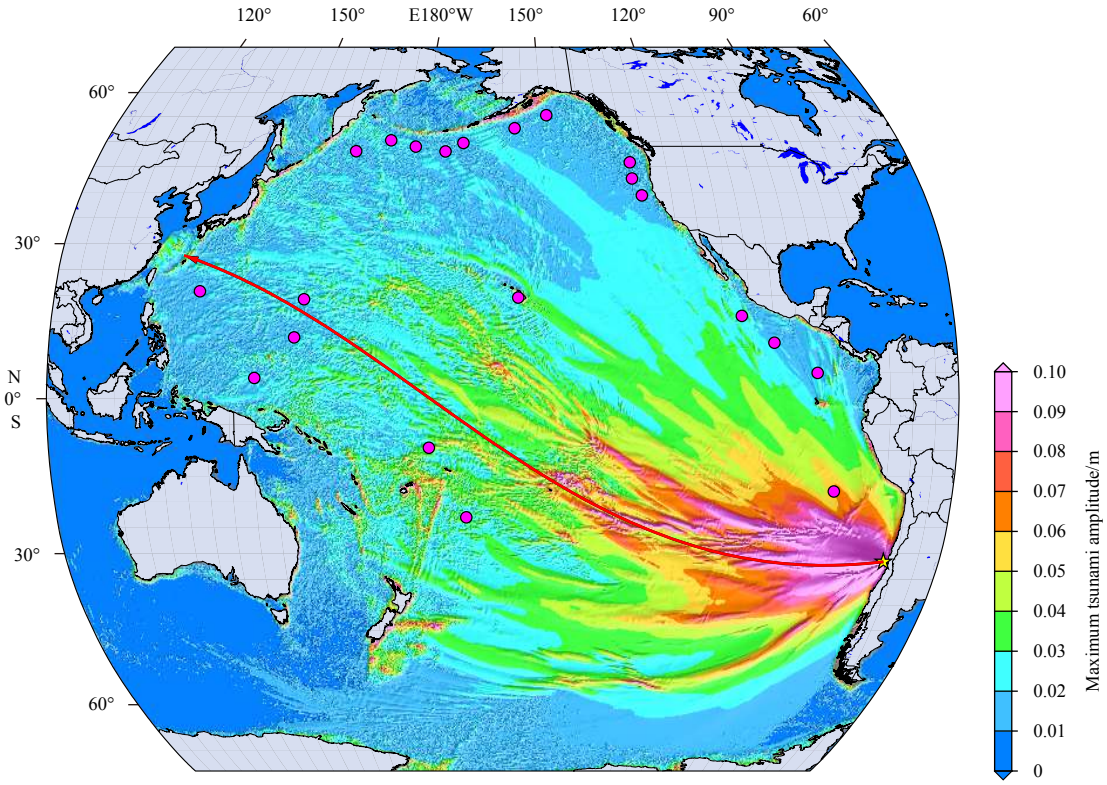

Fig. 6. Distribution of maximum simulated tsunami amplitude guided by seafloor topography and fault strike for the 2015 Illaple tsunami. Yellow star represents the epicenter. Solid circles indicate the locations of DART stations.

The tsunami propagation scenarios at three different moments based on the USGS finite fault model in the Pacific Ocean are described in Fig. 9. After generation off the coast of Chile, the tsunami spread across the Pacific Ocean. It then underwent refraction and diffraction when passing terrain features such as ridges, islands, and the continental shelf. Although it spread across the entire Pacific Ocean Basin, a tsunami with amplitude <5 cm is not enough to affect it. As shown in Fig. 9, the wavefields produced by the five corrected schemes looked similar at each time. After careful examination, however, we see that the leading negative phase is clearly observable in the snapshots presented in Column d and e of Fig. 9. The simulated LNP becomes increasingly significant with travel distance, as can be seen in this figure. The differences in tsunami amplitude are difficult to distinguish from a visual comparison of the wavefields. The comparison snapshots reveal that the tsunami wavefront propagation speed was reduced by the inclusion of elastic loading, wave dispersion, and seawater density stratification, or their coupling effect.

4.2 *Improved tsunami travel time delay*

Tsunami travel time delays between observations and linear long wave simulations have been reported as typical feature in recent transoceanic tsunami during their propagation in the deep ocean. From the comparison between observations and simulations (Figs 7 and 8), we can clearly see that travel time delays generally existed at the DART stations far from the epicenter. The arrival time of the first frontal crest wave is always referred for travel time delay investigation in this work. We estimated the travel time differences listed in Column 5 of Table 3 based on a visual selection of the first positive peaks. The DART is listed in order of distance from the epicenter. The travel time versus travel time delays and the ratio of travel time delays (T_d) to travel time (T_c) are plotted in Fig. 10, in order to better understand the features of the arrival time differences between observed and simulated waveforms based on the LSW equations at distant open-ocean stations. As shown in Fig. 10 and Table 3, the observed 2015 Chilean tsunami arrival times were delayed by 3–22 min relative to the simulated times, depending on the station location. An obvious linear correlation can be seen between the travel time and travel time delays (Fig. 10a). The correlation coefficient of the two datasets, r= 0.91, is closed to 1, indicating that the linear relationship is very strong. The dataset was fitted using the following fitting function for the relationship between the travel time and the travel time delays:

$$y = 0.97T_c - 2.6. \tag{7}$$

Theoretically, the linear relationship of Eq. (7) should pass through the origin of the coordinate system. Unfortunately, we had no available deep-ocean observation data within 2 000 km of the epicenter, there is a 2.6-h intercept on the x-axis based on the available data. From Figs 7, 8 and 10, some interesting points can be found at which tsunami simulations with travel times exceeding 2.6 h reported apparent travel time differences between simulations and observations. The differences increased with travel time or, equivalently, with distance from the source. The results also indicate that the tsunami speed decreased at stations far from the epicenter. The largest arrival time delay for the present event was 22 min (approximately 2% of the total travel time, as shown in Fig. 10b) observed at DART Sta. 52404 located more than 17 000 km from the source. We obtained results consistent with those reported by Heidarzadeh et al. (2015), i.e., larger

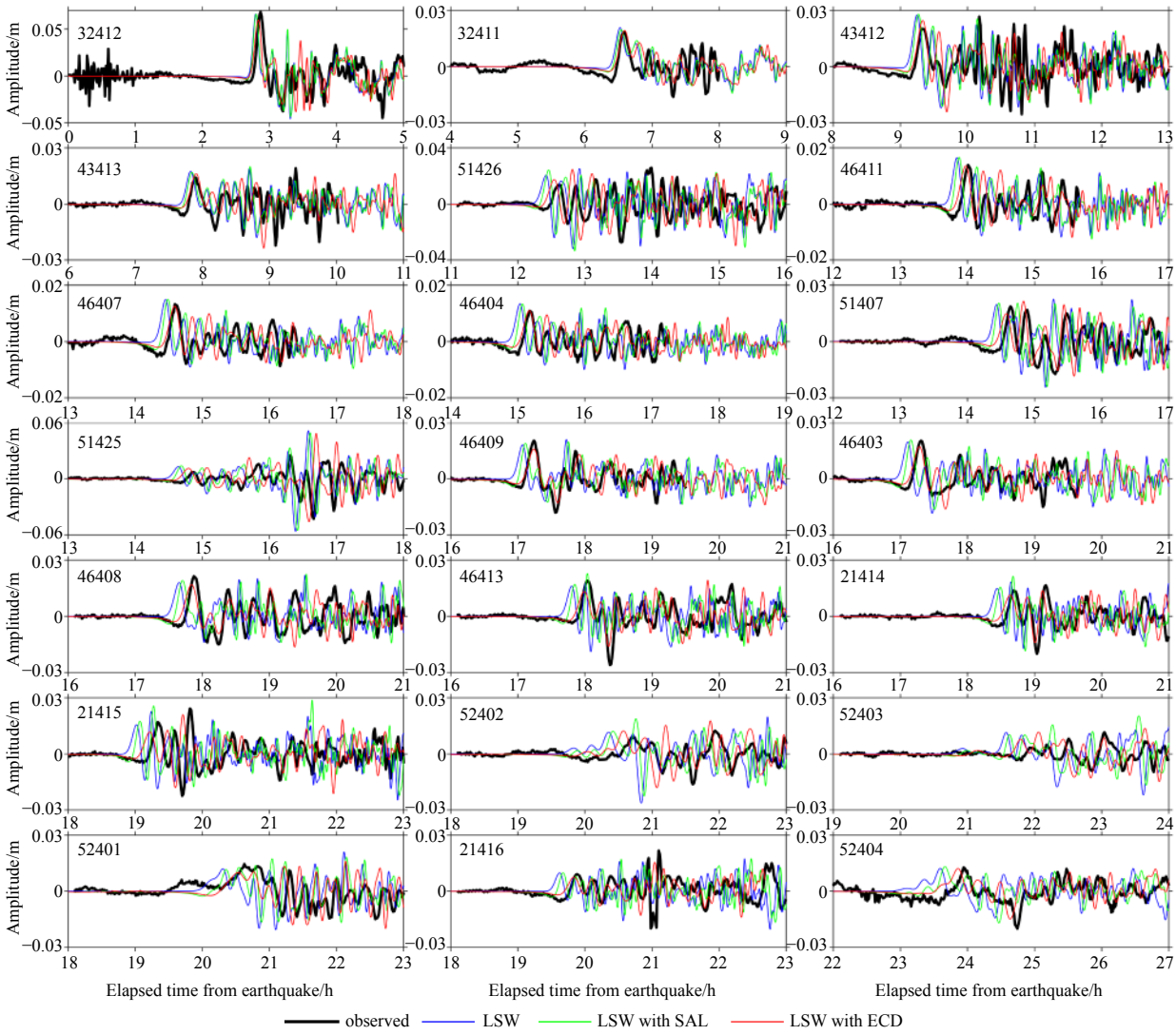

Fig. 7. Comparison of simulated waveforms with the observed DART records (black lines) for the 2015 Illapel tsunami. The blue lines indicate simulated tsunami by solving the LSW; the green lines indicate simulated tsunami with the effects of the elastic loading; and the red lines represent simulated tsunami with the coupling effects of elastic loading, seawater density stratification and wave dispersion.

delays usually appear to be concentrated around the direction normal to the fault strike.

The travel time delays at the far-field stations in the deep-ocean were attributed to the self-attraction and loading (SAL) effects associated with the mass motion during tsunami propagation, seawater density stratification, and wave dispersion (Watada et al., 2014; Poupardin et al., 2018). The present study attempted to reduce the travel time difference by considering each aforementioned physical effect and the combined effects. The improved travel time delays at the DART buoy stations are listed in Table 3. The numerical results of the corrected LSW equations indicate that the travel time differences were substantially reduced at all of the DARTs compared to the model run with the classical LSW equations. The trend of travel time delay as a function of travel time is still evident. The largest travel time delays between the observed and corrected simulated waveforms were reduced to approximately 8 min by taking into account the combined effects. In Column 9 of Table 3, we can see that the travel time delays have been reduced to zero at some of the DART stations. This study revealed that taking these effects into account results in more accurate phase speeds and arrival times, which agree with observations. Even though the travel time differences were improved overall by considering the secondary physical effects, there were significant differences between the simulated and observed arrival times at some stations. Thus, some aspects of the difference may be influenced by other effects that we do not yet understand.

Traditionally, we treat the ocean as an incompressible fluid with a rigid ocean floor. Such assumptions often lead to overestimation of the phase speed of tsunamis. The analysis carried out in this section confirms that taking the effects of SAL, seawater density stratification, and wave dispersion into account will result in more accurate phase speeds and arrival times. To better understand the secondary physical effects to what extent the travel time delay can be affected, we plotted these improved travel time delays against the delays relative to the LSW simulations (T_d) in Fig. 11a. The different colored solid lines represent the fitting relationship of each corrected travel time delay to T_d.

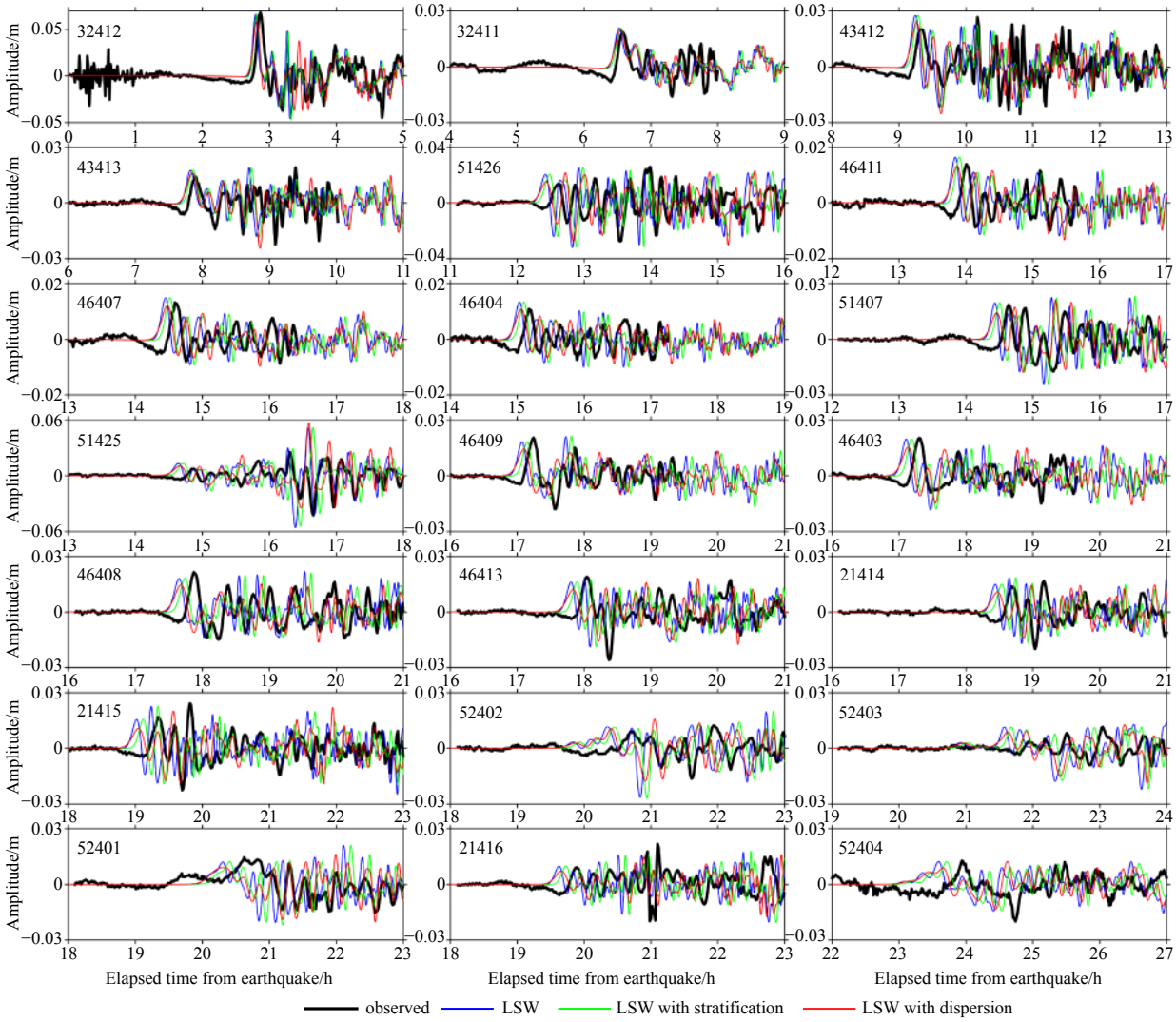

Fig. 8. Comparison of simulated waveforms with the observed DART records (black lines) for the 2015 Illapel tsunami. The blue lines indicate simulated tsunami by solving the LSW. The green lines indicate simulated tsunami with the effect of the seawater density stratification. The red lines represent simulated tsunami with the wave dispersion.

The fitting functions have also been included in Fig. 11a. The slope of the fitting curve indicates the rate of change for the corrected travel time delays over T_d. The smaller the rate of change, the more significant the effect on the delay improvement. As shown in Fig. 11a, the slopes of the fitted curves are not greater than 1. This means that all of the physical effects and their coupling effects effectively reduced the travel time errors compared to the traditional LSW simulation results. Among the five simulation schemes carried out in this study, the scheme that comprehensively considered the effects of SAL, wave dispersion and seawater density stratification obtained the most accurate tsunami travel time. Seawater density stratification was found to play the most significant role in improving travel time delays among the three physical effects. Generally, the scheme including the SAL effect produced a more accurate travel time than the scheme considering wave dispersion. However it is worth noting that this advantage of improving travel time delays did not appear until nearly 10 h after the tsunami began propagating. This further proves that wave dispersion, the earth's elasticity, and density stratification are not significant in the near field. To demonstrate the improvement efficiency of different simulated schemes, the delays differences between the improved travel time delay and T_d as functions of travel time (T_c) are plotted in Fig. 11b. The different colored solid lines represent the fitting relationship of each corrected delay difference to travel time, as shown in Fig. 11a. The slopes of the curves indicate how fast the delay improvement varies with travel time. Unlike the slopes in Fig. 11a, the larger the slope of the fitted curve in Fig. 11b, the greater the improvement efficiency of the physical effect on the travel time delay. The simulated results considering the combined effects exhibited the greatest improvement efficiency on the travel time delay. Figure 11b reveals that the correction due to seawater density stratification displayed the fastest reduction of travel time difference with increasing travel time. The effects of SAL and wave dispersion exerted relatively mild effects on decreasing travel time differences with travel time. The travel time delay differences due to wave dispersion were larger than the corrections due to SAL in the near field, while the opposite was found in the far field. Further research and data analysis are necessary to determine possible causes.

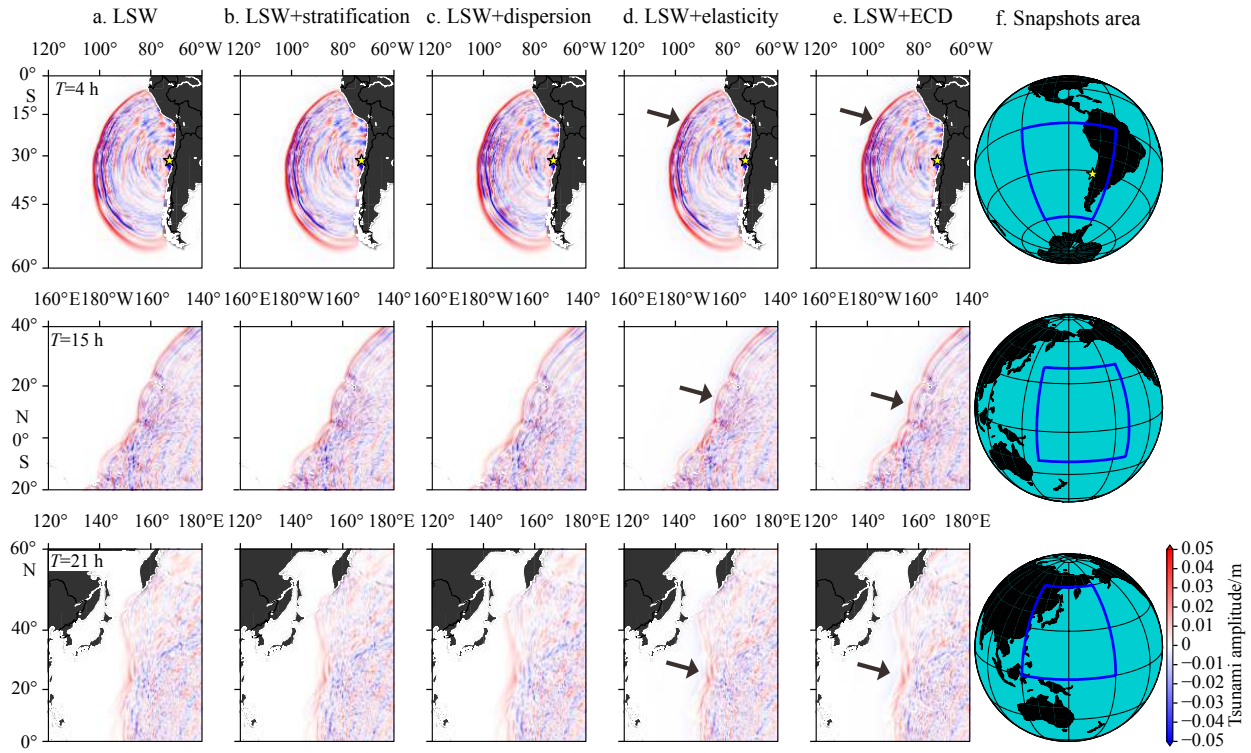

Fig. 9. Comparison of the LSW simulated tsunami propagation snapshots with corrected LSW simulations in the Pacific Ocean at 4 h, 15 h and 21 h after the earthquake. Column a shows the tsunami wavefields simulated by solving the LSW model, Column b shows the corrected tsunami wavefields simulated by taking into account the effect seawater density stratification, Column c shows the simulated tsunami wavefields with a correction for wave dispersion, Column d shows the simulated tsunami wavefields with SAL correction, Column e represents the simulated tsunami wavefield with coupled ECD correction, and Column f depicts the snapshots display area of tsunami propagation at corresponding moment. The positions of black arrow indicate the LNP arriving.

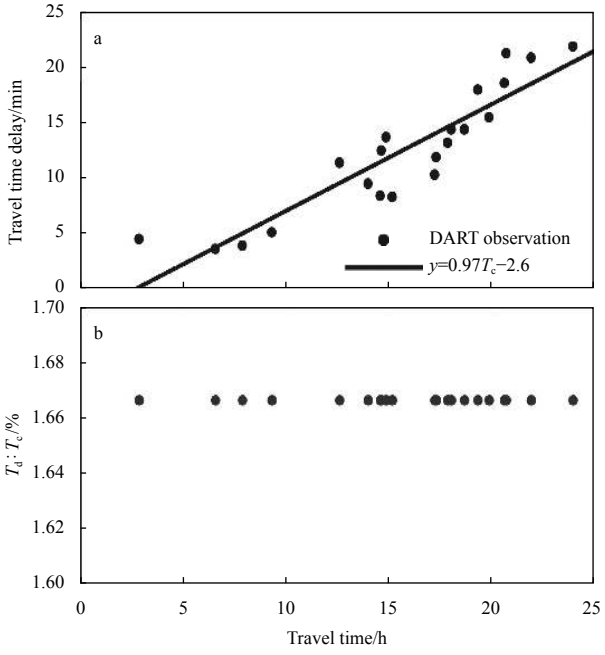

Fig. 10. The travel time delays as function of the tsunami travel time across the Pacific Ocean (a), and the relationship between the ratio of T_d to T_c and travel time based on available deep-ocean data (b). The black circles in a are the available DART observed travel time delays relative to the numerically simulated long waves.

Together, the three effects are able to explain the majority of the difference between the observed and simulated arrival times for the 2015 Chilean tsunami. To quantitatively estimate the contribution of SAL due to the earth's elastic loading, seawater density stratification due to compressibility, and wave dispersive effects on the travel time delay improvement, the contribution rate was defined as the percentage value of the corrected time delay difference for each effect relative to T_d at 21 DART stations. The results are plotted in Fig. 12. This figure shows that the order of the contribution rate of each physical effect on travel time delay correction was consistent, with the exceptions of DART Stas 32411 and 32412 in the near field. In agreement with An and Liu (2016) and Ho et al. (2017), we conclude that the ECD combined effects scheme accounted for approximately 78% on average of the travel time delays at the deep-ocean stations, with seawater density stratification accounting for approximately 39% on average, the SAL effect due to the earth's elastic loading accounting for approximately 21% on average, and wave dispersion contributing approximately 18% on average.

4.3 *Comparative spatial influence on tsunami waves*

The simulated tsunami waveforms successfully reproduced the characteristics of the observed tsunami waveforms, including the travel time delay and small initial negative phase before the main peak at specific locations. To investigate the spatiotemporal impacts of secondary physical effects on tsunami characteristics, Figs 13 and 14 summarize the synoptic results in terms of the percent change of the maximum wave amplitude and wavefront arrival time when the numerical model included each

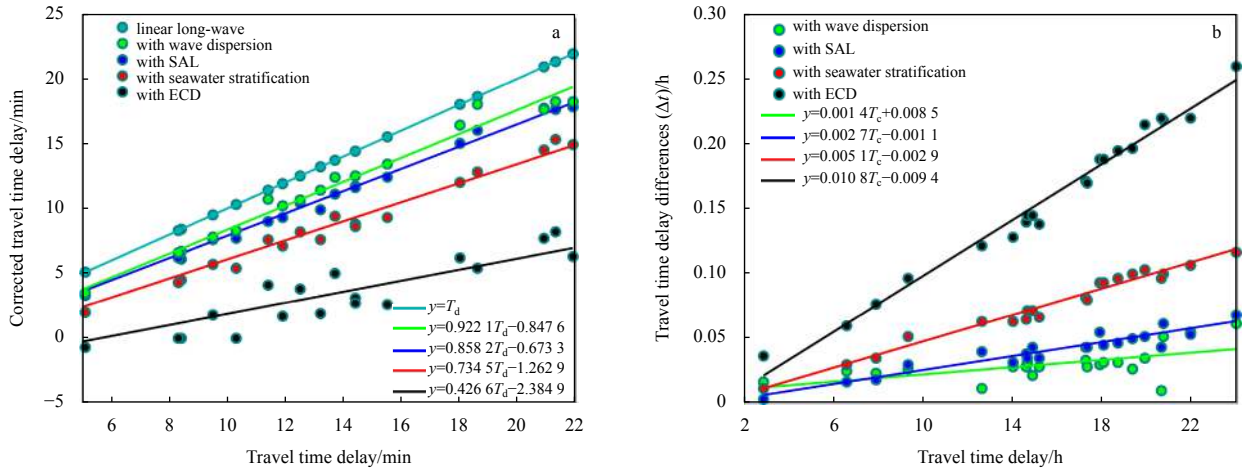

Fig. 11. Evaluation the impact of different correction schemes for improving tsunami travel time delay. a. Comparison of travel time delays between observed waveforms relative to the LSW simulations and corrected travel time delay at each DART station. b. The travel time delay differences between improved travel time delay and T_d as functions of travel time (T_c).

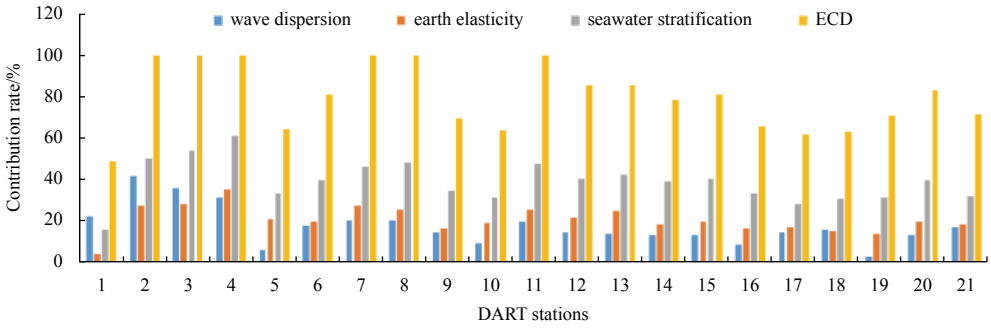

Fig. 12. The contribution rate for improving travel time delay using different correction schemes. Comparison the impact of SAL, seawater density stratification due to compressibility, physical dispersion and the coupling effects (ECD) on tsunami travel time delay corrections.

secondary physical effect individually. In terms of maximum tsunami amplitude, Fig. 13a presents the synoptic results with percent change due to seawater density stratification effect. The stratification effect exerted almost no significant impact on tsunami wave amplitude along the propagation directions. In addition, there was no net overall tendency toward increased or reduced wave amplitude in the far field. In contrast, the SAL effects resulted in an enhancement of tsunami amplitude along the main propagation direction, except the boundary channel (Fig. 13b). The percent change due to SAL effects were on the order of a few percent at most in the near field, with maximum differences on the order of ±10%. There was no uniform tendency exhibited due to SAL over the entire Pacific Ocean Basin. Figure 13c illustrates the Boussinesq dispersion effects for the 2015 Chilean tsunami event, showing the percent change between the simulated results with and without dispersion effects. Pronounced dispersion effects on tsunami amplitude distribution were observed along the major propagation directions. There was an overall tendency for the dispersion simulation to lead to a reduction of maximum tsunami amplitude within the reach of the tsunami waves, but as noted by Kirby et al. (2013), these effects may be partially reversed in the far field. The maximum difference between the two results was approximately 30%, as can be seen in Fig. 13c. The dispersion effects became important after the tsunami had traveled more than several thousand kilometers. Figure 13d shows the influence of all the secondary physical effects on maximum tsunami amplitude distribution in term of percent change. The percent change was on the order of 20% in the near field along the major propagation directions. This result indicates that the combined effects lead to smaller tsunami waves in the near field. This effect is partially reversed in the far field, similar to the dispersion effect, since it is caused by the superposition of dispersion and SAL effects. It was also proved that the influence of dispersion on the maximum amplitude is stronger than the SAL effect.

In terms of tsunami arrival time, Fig. 14 displays the tsunami arrival times difference between the corrected LSW and the standard LSW solution. Each panel reveals that the corrections can reduce the tsunami propagation speed. The differences increased with travel time from 0 min to 5 min. This result is consistent with previous analysis. The differences were mainly distributed in the major direction of tsunami propagation. It is worth noting that there were two high-difference regions, one in the Northwest Pacific Ocean, and the other in the Southwest Pacific Ocean (Figs 14a and b). This type of region only appeared in the corrected scheme that could change the tsunami waveform simulations, such as changes due to wave dispersion, SAL, or ECD effects. It is proposed that this occurrence may be due to phase picking error automatically when determining the arrival time of the first frontal crest tsunami wave in areas with complex

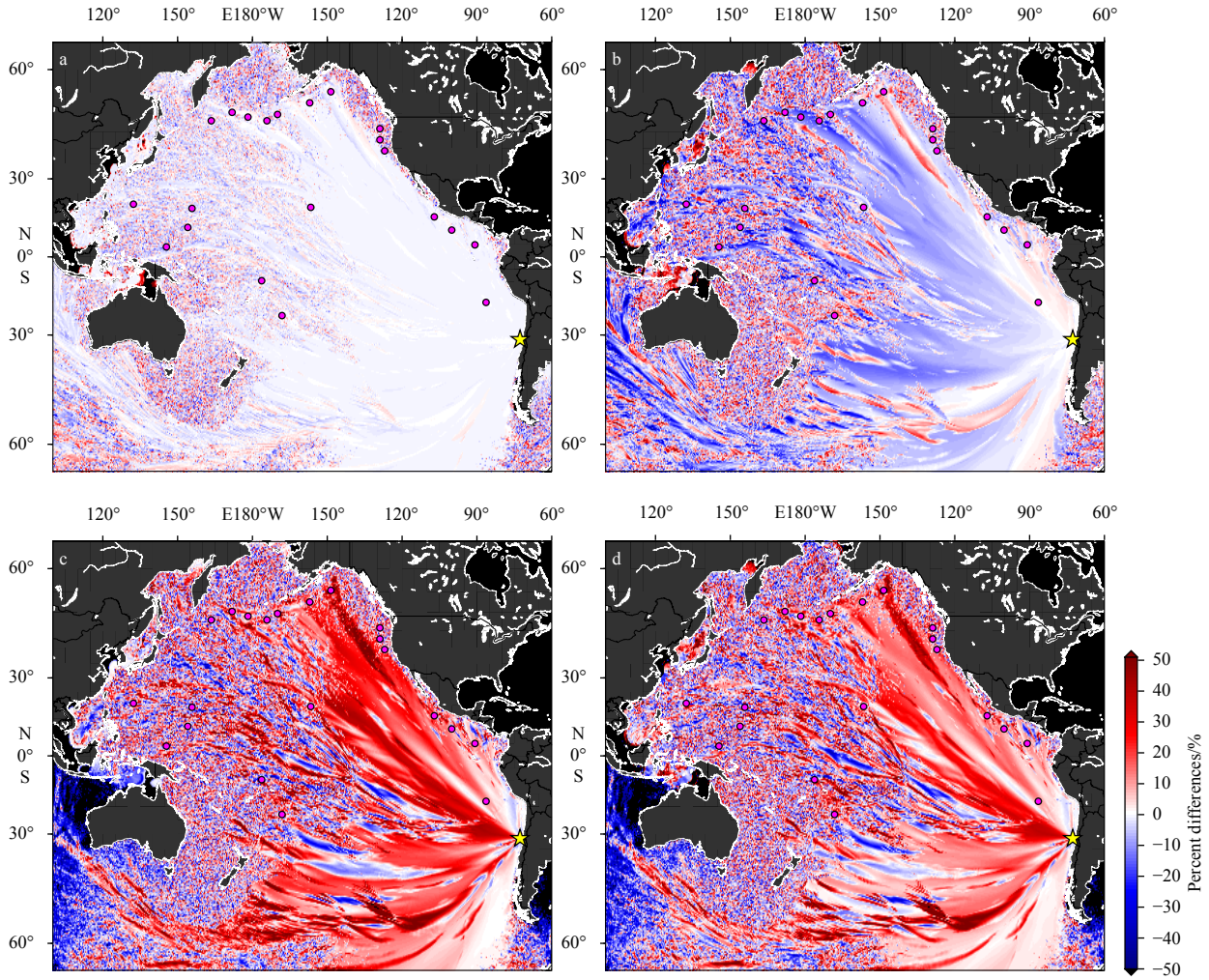

Fig. 13. Percent differences of simulated maximum amplitude for the 2015 Chilean tsunami between with and without corrected models. a. Percent change between the LSW results and the corrected LSW simulations by coupling the seawater density stratification due to compressibility effect, b. percent change between the LSW results and the corrected LSW simulations by coupling the SAL effect, c. percent difference between the LSW results and the corrected LSW taking into account the effect of wave dispersion, and d. percent change between the LSW and the corrected LSW that includes the effects of the SAL, stratification and physical dispersion.

waveform and terrain. Because the seawater density stratification due to compressibility cannot change the tsunami waveform, Fig. 14c presents a smooth result, which has a better reference value. Nevertheless, for the most of simulation area, the delay improvement efficiency of each effect is also consistent with previous observations and analyses.

5 Discussion and conclusions

Comparing the observations of recent tsunami events with predictions based on the standard shallow water equations during tsunami propagation in the deep ocean revealed that systematic discrepancies exist in both tsunami arrival time and initial phase polarity. Systemic travel time discrepancy between observed and simulated waveforms can be up to 20 min when a tsunami travels more than 10 000 km from its sources. In addition to the discrepancy in arrive time, a small leading negative phase with a long period preceding the first elevated wave is commonly found at far-field stations. The inadequate fit between the modeled and observed waveforms has often been attributed to the limited resolution of the bathymetry data, nonlinear effects, bottom friction, grid size, and other factors. Relevant studies have shown, however, that the aforementioned possible reasons do not account for the observed systematic differences, especially in the far field.

In this work, the systematic discrepancies were identified for the recent 16 September 2015 Illapel, Chile transoceanic tsunami event by examining the wave characteristics from the tsunami records of 21 DART sites and 29 coastal tide gauge stations. The analysis and examination of the records from the various stations focused on summarizing the quantitative characteristics and validating the repeatability of the systematic discrepancies. The results demonstrate that systematic tsunami travel time delays of as much as 22 min (approximately 1.7% of the total travel time) occurred in the 2015 Chilean tsunami far-field propagation of more than 15 000 km. The delay discrepancy was found to increase with travel time. Our findings are in good agreement with, and support, the theoretical results. We also discovered that it was difficult to identify the LNP from the nearshore observation system due to the strong background noise, although the initial negative phase feature became more promin-

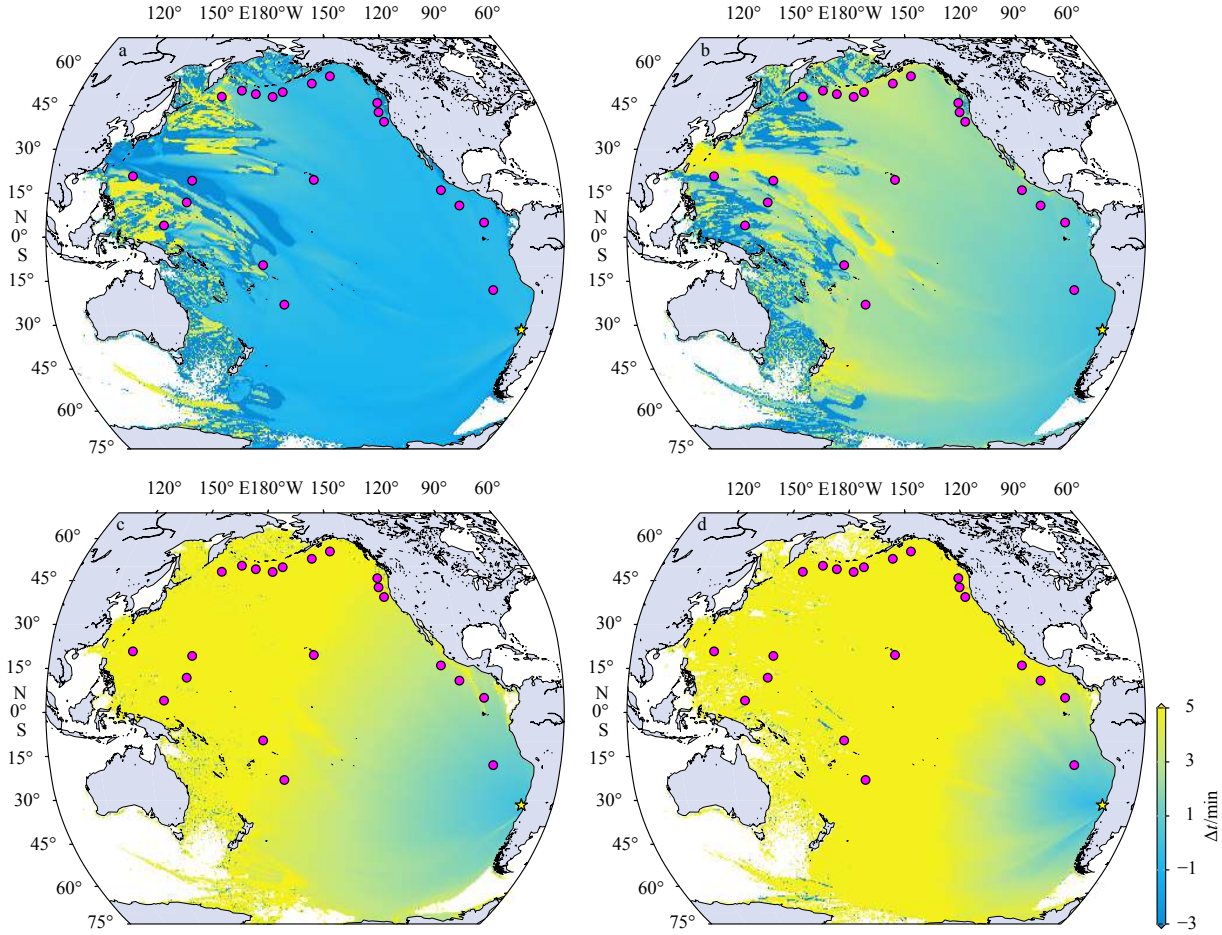

Fig. 14. Tsunami arrival time differences (Δt) between estimated corrected LSW simulations and LSW solvers. a. Arrival time difference between the simulated tsunami that take into account dispersion effects and the LSW results, b. arrival time difference between the simulated tsunami with a correction for elasticity of solid Earth and the LSW results, c. arrival time difference between the simulation that take into account seawater stratification and the LSW results, and d. arrival time difference between the simulation that take into account the effects of ECD and the LSW results.

ent as the tsunami propagated from the source area into the deep ocean. A LNP was found for the Chile tsunami with an average duration of 33 min, which is close to the dominant period of the tsunami source. Most of the amplitude ratios to the first elevation phase were approximately 40%, with the largest equivalent to the first positive phase amplitude. The magnification of the LNP feature away from the tsunami source indicated that leading negative waves are identifiable features that should not be attributed solely to source characteristics. The results once again demonstrate that a negative phase preceding a major arriving frontal crest wave is a consistent feature of transoceanic tsunamis.

We employed the revised shallow water equations model to accurately calculate the arrival time and LNP to evaluate the specific impacts of the secondary physical effects on the discrepancies of a moderate transoceanic tsunami event. Taking all these effects into consideration, we can conclude that the corrected shallow water model can reproduce the characteristics of the observed tsunami waveforms, including the travel time delay and small initial negative phase before the main peak at distant locations. The travel time delay between the observed and corrected simulated waveforms was reduced to <8 min and the amplitude discrepancy between them was also greatly diminished. The incorporating effects amounted to approximately 78% of the travel time delay correction, with seawater density stratification, SAL, and Boussinesq dispersion contributing approximately 39%, 21%, and 18%, respectively. The simulated results revealed that the elastic loading and Boussinesq dispersion not only affected the travel time but also changed the simulated waveforms of this event. In contrast, the seawater density stratification due to compressibility only reduced the tsunami speeds, whereas the earth's elasticity was responsible for the LNP due to the depression of the seafloor surrounding the additional tsunami loading at the far-field stations. Therefore, it was necessary to utilize the corrected shallow water model to describe accurately the tsunami propagation features by considering the secondary physical effects. The results of this study support previous theory and help to explain the observed discrepancies.

The effects considered in this work did not account for all discrepancies between the observed and simulated tsunami waveforms described herein, which may be due to possible errors in model initialization, as well as other unknown reasons. The effects of SAL, seawater density stratification, and wave dispersion, however, did reduce the tsunami waveform misfitting, and we could further employ these data to identify and correct the other error sources. In terms of promoting tsunami early warning and mitigation system, the authors suggest that accurately estimating

the arrival time and magnitude of the leading waves by considering typically neglected effects is essential when utilizing inverse modeling and forecasting systems to minimize potential losses of buildings, property, and lives. For scientific research, these effects should also all be considered to accurately reproduce the physical processes of tsunami propagation and to facilitate the investigation of the disaster-causing mechanisms of tsunami waves.

Acknowledgements

The tide gauge and DART data were downloaded from the Intergovernmental Oceanographic Commission (IOC) website (http://www.ioc-sealevelmonitoring.org) and the National Oceanic and Atmospheric Administration (NOAA) website (http://www.ndbc.noaa.gov/dart.shtml), respectively. Some figures were prepared using Generic Mapping Tools (GMT; Wessel and Smith, 1998) and MATLAB software. We utilized the JAGURS tsunami simulation code (available at https://github.com/jagurs-admin).

References

Abdolali A, Kadri U, Kirby J T. 2019. Effect of water compressibility, sea-floor elasticity, and field gravitational potential on tsunami phase speed. Scientific Reports, 9(1): 16874, doi: 10.1038/s41598-019-52475-0

Abdolali A, Kirby J T. 2017. Role of compressibility on tsunami propagation. Journal of Geophysical Research: Oceans, 122(12): 9780–9794, doi: 10.1002/2017JC013054

Allgeyer S, Cummins P. 2014. Numerical tsunami simulation including elastic loading and seawater density stratification. Geophysical Research Letters, 41(7): 2368–2375, doi: 10.1002/2014GL059348

An Chao, Liu P L F. 2016. Analytical solutions for estimating tsunami propagation speeds. Coastal Engineering, 117: 44–56, doi: 10.1016/j.coastaleng.2016.07.006

Aránguiz R, González G, González J, et al. 2016. The 16 September 2015 Chile tsunami from the post-tsunami survey and numerical modeling perspectives. Pure and Applied Geophysics, 173(2): 333–348, doi: 10.1007/s00024-015-1225-4

Baba T, Allgeyer S, Hossen J, et al. 2017. Accurate numerical simulation of the far-field tsunami caused by the 2011 Tohoku earthquake, including the effects of Boussinesq dispersion, seawater density stratification, elastic loading, and gravitational potential change. Ocean Modelling, 111: 46–54, doi: 10.1016/j.ocemod.2017.01.002

Baba T, Ando K, Matsuoka D, et al. 2016. Large-scale, high-speed tsunami prediction for the great Nankai Trough earthquake on the K computer. The International Journal of High Performance Computing Applications, 30(1): 71–84, doi: 10.1177/1094342015584090

Baba T, Cummins P R, Thio H K, et al. 2009. Validation and joint inversion of teleseismic waveforms for earthquake source models using deep ocean bottom pressure records: A case study of the 2006 Kuril megathrust earthquake. Pure and Applied Geophysics, 166(1-2): 55–76, doi: 10.1007/s00024-008-0438-1

Baba T, Takahashi N, Kaneda Y, et al. 2015. Parallel implementation of dispersive tsunami wave modeling with a nesting algorithm for the 2011 Tohoku tsunami. Pure and Applied Geophysics, 172(12): 3455–3472, doi: 10.1007/s00024-015-1049-2

Barazangi M, Isacks B L. 1976. Spatial distribution of earthquakes and subduction of the Nazca plate beneath South America. Geology, 4(11): 686–692, doi: 10.1130/0091-7613(1976)4<686:SDOEAS>2.0.CO;2

Berger M J, George D L, Leveque R J, et al. 2011. The GeoClaw software for depth-averaged flows with adaptive refinement. Advances in Water Resources, 34(9): 1195–1206, doi: 10.1016/j.advwatres.2011.02.016

Contreras-López M, Winckler, P, Sepúlveda I, et al. 2016. Field survey of the 2015 Chile tsunami with emphasis on coastal wetland and conservation areas. Pure and Applied Geophysics, 173(2): 349–367, doi: 10.1007/s00024-015-1235-2

DeMets C, Gordon R G, Argus D F, et al. 1994. Effect of recent revisions to the geomagnetic reversal time scale on estimates of current plate motions. Geophysical Research Letters, 21(20): 2191–2194, doi: 10.1029/94GL02118

Eblé M C, Mungov G T, Rabinovich A B. 2015. On the leading negative phase of major 2010-2014 tsunamis. Pure and Applied Geophysics, 172(12): 3493–3508, doi: 10.1007/s00024-015-1127-5

Heidarzadeh M, Murotani S, Satake K, et al. 2016. Source model of the 16 September 2015 Illapel, Chile, M_w8.4 earthquake based on teleseismic and tsunami data. Geophysical Research Letters, 43(2): 643–650, doi: 10.1002/2015GL067297

Heidarzadeh M, Satake K. 2013. Waveform and spectral analyses of the 2011 Japan tsunami records on tide gauge and DART stations across the Pacific Ocean. Pure and Applied Geophysics, 170(6–8): 1275–1293, doi: 10.1007/s00024-012-0558-5

Heidarzadeh M, Satake K. 2014. The El Salvador and Philippines tsunamis of August 2012: insights from sea level data analysis and numerical modeling. Pure and Applied Geophysics, 171(12): 3437–3455, doi: 10.1007/s00024-014-0790-2

Heidarzadeh M, Satake K, Murotani S, et al. 2015. Deep-water characteristics of the trans-Pacific tsunami from the 1 April 2014 M_w8.2 Iquique, Chile earthquake. Pure and Applied Geophysics, 172(3–4): 719–730, doi: 10.1007/s00024-014-0983-8

Heidarzadeh M, Satake K, Takagawa T, et al. 2018. A comparative study of far-field tsunami amplitudes and ocean-wide propagation properties: insight from major trans-Pacific tsunamis of 2010–2015. Geophysical Journal International, 215(1): 22–36, doi: 10.1093/gji/ggy265

Ho T C, Satake K, Watada S. 2017. Improved phase corrections for transoceanic tsunami data in spatial and temporal source estimation: application to the 2011 Tohoku earthquake. Journal of Geophysical Research: Solid Earth, 122(12): 10155–10175, doi: 10.1002/2017JB015070

Inazu D, Saito T. 2013. Simulation of distant tsunami propagation with a radial loading deformation effect. Earth Planets Space, 65(8): 835–842, doi: 10.5047/eps.2013.03.010

Jakeman J D, Nielsen O M, Putten K V, et al. 2010. Towards spatially distributed quantitative assessment of tsunami inundation models. Ocean Dynamics, 60(5): 1115–1138, doi: 10.1007/s10236-010-0312-4

Ji Chen, Wald D J, Helmberger D V. 2002. Source description of the 1999 hector mine, California, earthquake, part I: wavelet domain inversion theory and resolution analysis. Bulletin of the Seismological Society of America, 92(4): 1192–1207, doi: 10.1785/0120000916

Kajiura K. 1963. The leading wave of a tsunami. Bulletin of the Earthquake Research Institute, University of Tokyo, 41(3): 535–571

Kato T, Terada Y, Nishimura H, et al. 2011. Tsunami records due to the 2010 Chile Earthquake observed by GPS buoys established along the Pacific coast of Japan. Earth, Planets and Space, 63(6): e5–e8, doi: 10.5047/eps.2011.05.001

Kirby J T, Shi Fengyan, Tehranirad B, et al. 2013. Dispersive tsunami waves in the ocean: model equations and sensitivity to dispersion and Coriolis effects. Ocean Modelling, 62: 39–55, doi: 10.1016/j.ocemod.2012.11.009

Li Bo, Ghosh A. 2016. Imaging rupture process of the 2015 M_w 8.3 Illapel earthquake using the US seismic array. Pure and Applied Geophysics, 173(7): 2245–2255, doi: 10.1007/s00024-016-1323-y

Lu W F, Jiang Y W, Lin J. 2013. Modeling propagation of 2011 Honshu tsunami. Engineering Applications of Computational Fluid Mechanics, 7(4): 507–518, doi: 10.1080/19942060.2013.11015489

Okada Y. 1985. Surface deformation due to shear and tensile faults in a half-space. Bulletin of the Seismological Society of America, 75(4): 1135–1154, doi: 10.1785/BSSA0750041135

Poupardin P, Heinrich P, Hébert H, et al. 2018. Traveltime delay relative to the maximum energy of the wave train for dispersive tsunamis propagating across the Pacific Ocean: the case of 2010 and 2015 Chilean Tsunamis. Geophysical Journal International,

214(3): 1538–1555, doi: 10.1093/gji/ggy200
Prastowo T, Cholifah L, Madlazim. 2018. Analysis of travel time delay for large tsunamis across the pacific and Indian Oceans. Science of Tsunami Hazards, 37(4): 195–212
Rabinovich A B, Candella R N, Thomson R E. 2013a. The open ocean energy decay of three recent trans-Pacific tsunamis. Geophysical Research Letters, 40(12): 3157–3162, doi: 10.1002/grl.50625
Rabinovich A B, Thomson R E. 2007. The 26 December 2004 Sumatra tsunami: analysis of tide gauge data from the World Ocean Part 1. Indian Ocean and South Africa. Pure and Applied Geophysics, 164(2): 261–308, doi: 10.1007/s00024-006-0164-5
Rabinovich A B, Thomson R E, Fine I V. 2013b. The 2010 Chilean tsunami off the west coast of Canada and the northwest coast of the United States. Pure and Applied Geophysics, 170(9-10): 1529–1565, doi: 10.1007/s00024-012-0541-1
Rabinovich A B, Titov V V, Moore C W, et al. 2017. The 2004 Sumatra tsunami in the southeastern Pacific Ocean: New global insight from observations and modeling. Journal of Geophysical Research: Oceans, 122(10): 7992–8019, doi: 10.1002/2017JC013078
Rabinovich A B, Woodworth P L, Titov V V. 2011. Deep-sea observations and modeling of the 2004 Sumatra tsunami in Drake Passage. Geophysical Research Letters, 38(16): L16604, doi: 10.1029/2011GL048305
Roberts S G, Nielsen O M, Gray D, et al. 2015. ANUGA User Manual, Release 2.0. Symonston: Geoscience Australia, https://www.researchgate.net/publication/318511561_ANUGA_User_Manual_Release_20 [2015-05-19/2020-10-01]
Roberts S G, Nielsen O M, Jakeman J. 2008. Simulation of tsunami and flash floods. In: Bock H G, Kostina E, Phu H X, et al., eds. Modeling, Simulation and Optimization of Complex Processes. Berlin, Heidelberg: Springer, doi: 10.1007/978-3-540-79409-7_35
Röbke B R, Vött A. 2017. The tsunami phenomenon. Progress in Oceanography, 159: 296–322, doi: 10.1016/j.pocean.2017.09.003
Satake K, Heidarzadeh M. 2017. A review of source models of the 2015 Illapel, Chile earthquake and insights from tsunami data. Pure and Applied Geophysics, 174(1): 1–9, doi: 10.1007/s00024-016-1450-5
Shan Di, Wang Peitao, Ren Zhiyuan, et al. 2017. Application and evaluation of the 16 September 2015 Illapel, Chile M_w8.3 earthquake finite fault rupture model from numerical simulation. Haiyang Xuebao (in Chinese), 39(11): 49–60, doi: 10.3969/j.issn.0253-4193.2017.11.005
Tang Liujuan, Titov V V, Moore C, et al. 2016. Real-time assessment of the 16 September 2015 Chile tsunami and implications for near-Field forecast. Pure and Applied Geophysics, 173(2): 369–387, doi: 10.1007/s00024-015-1226-3
Titov V V, Synolakis C E. 1998. Numerical modeling of tidal wave runup. Journal of Waterway, Port, Coastal, and Ocean Engineering, 124(4): 157–171, doi: 10.1061/(ASCE)0733-950X(1998)124:4(157)
Tsai V C, Ampuero J P, Kanamori H, et al. 2013. Estimating the effect of earth elasticity and variable water density on tsunami speeds. Geophysical Research Letters, 40(3): 492–496, doi: 10.1002/grl.50147
Vigny C, Rudloff A, Ruegg J C, et al. 2009. Upper plate deformation measured by GPS in the Coquimbo Gap, Chile. Physics of the Earth and Planetary Interiors, 175(1–2): 86–95, doi: 10.1016/j.pepi.2008.02.013
Wang Dailin. 2015. An ocean depth-correction method for reducing model errors in tsunami travel time: application to the 2010 Chile and 2011 Tohoku tsunamis. Science of Tsunami Hazards, 34(1): 1–22
Wang Dailin, Becker N C, Walsh D, et al. 2012. Real-time forecasting of the April 11, 2012 Sumatra tsunami. Geophysical Research Letters, 39(19): L19601, doi: 10.1029/2012GL053081
Wang Xiaoming, Liu P L F. 2011. An explicit finite difference model for simulating weakly nonlinear and weakly dispersive waves over slowly varying water depth. Coastal Engineering, 58(2): 173–183, doi: 10.1016/j.coastaleng.2010.09.008
Wang Peitao, Yu Fujiang, Yuan Ye, et al. 2016. Effects of finite fault rupture models of submarine earthquakes on numerical forecasting of near-field tsunami. Chinese Journal Of Geophysics (in Chinese), 59(3): 1030–1045, doi: 10.6038/cjg20160324
Watada S. 2013. Tsunami speed variations in density-stratified compressible global oceans. Geophysical Research Letters, 40(15): 4001–4006, doi: 10.1002/grl.50785
Watada S, Kusumoto S, Satake K. 2014. Traveltime delay and initial phase reversal of distant tsunamis coupled with the self-gravitating elastic earth. Journal of Geophysical Research: Solid Earth, 119(5): 4287–4310, doi: 10.1002/2013JB010841
Wei Yong, Bernard E N, Tang Liujuan, et al. 2008. Real-time experimental forecast of the Peruvian tsunami of August 2007 for U.S. Coastlines. Geophysical Research Letters, 35(4): L04609, doi: 10.1029/2007GL032250
Wessel P, Smith W H F. 1998. New, improved version of generic mapping tools released. Eos, Transactions American Geophysical Union, 79(47): 579, doi: 10.1029/98EO00426
Yamazaki Y, Cheung K F, Kowalik Z. 2011. Depth-integrated, non-hydrostatic model with grid-nesting for tsunami generation, propagation, and run-up. International Journal for Numerical Methods in Fluids, 67(12): 2081–2107, doi: 10.1002/fld.2485
Yamazaki Y, Cheung K F, Lay T. 2013. Modeling of the 2011 Tohoku near-field tsunami from finite-fault inversion of seismic waves. Bulletin of the Seismological Society of America, 103(2B): 1444–1455, doi: 10.1785/0120120103
Ye Lingling, Lay T, Kanamori H, et al. 2016. Rapidly estimated seismic source parameters for the 16 September 2015 Illapel, Chile M_w8.3 earthquake. Pure and Applied Geophysics, 173(2): 321–332, doi: 10.1007/s00024-015-1202-y
Zaytsev O, Rabinovich A B, Thomson R E. 2016. A comparative analysis of coastal and open-ocean records of the great Chilean tsunamis of 2010, 2014 and 2015 off the coast of Mexico. Pure and Applied Geophysics, 173(12): 4139–4178, doi: 10.1007/s00024-016-1407-8
Zaytsev O, Rabinovich A B, Thomson R E. 2017. The 2011 Tohoku tsunami on the coast of Mexico: A case study. Pure and Applied Geophysics, 174(8): 2961–2986, doi: 10.1007/s00024-017-1593-z